Nanoscale

PAPER

View Article Online
View Journal | View Issue

Cite this: *Nanoscale*, 2026, **18**, 4258

Nanoindentation-induced subsurface phase engineering in oxide-capped silicon

Megha Sasidharan Nisha *[a] and Kiran Mangalampalli *[b]

The controlled formation of high-pressure silicon polymorphs beneath an oxide layer offers a new paradigm for subsurface phase engineering. We systematically compared sharp Berkovich and spherical nanoindentation on 285 nm SiO_2-capped Si(100) using Raman spectroscopy and cross-sectional electron microscopy to reveal how contact geometry and oxide constraint govern phase transformation. Sharp indentation initiates R8 (rhombohedral)/BC8 (body-centered-cubic) phase formation at low loads (42 mN), but the high stress concentration promotes early oxide fracture and radial cracking, limiting the continuous crystalline volume. In contrast, spherical indentation delays observable transformation until ~92 mN, distributing stress more uniformly. Crucially, we identify a "critical loading window" for optimization. While moderate spherical loads (~200 mN) facilitate highly ordered crystalline recovery with intact interfaces, excessive loads (~500 mN) exceed the oxide's confinement capacity, favoring collapse into a disordered amorphous state and localized fracture due to the significant volumetric expansion of the intermediate β-Sn phase. Our results confirm that the oxide modulates stress-relaxation kinetics without altering the fundamental 11–12 GPa transformation threshold. These findings explicitly define the operational limits for dielectric confinement, providing a versatile pathway for engineering subsurface crystalline phases with enhanced carrier mobility and sub-bandgap optical absorption for next-generation silicon photonic and sensing platforms.

Received 26th September 2025,
Accepted 7th January 2026

DOI: 10.1039/d5nr04069h

rsc.li/nanoscale

1. Introduction

Nanoindentation has emerged as a powerful tool to probe the complex mechanical response of silicon, a quintessential semiconductor material.[1–3] Although monocrystalline silicon is brittle under ambient conditions, it undergoes dramatic pressure-induced phase transformations that can enable ductile-like deformation under the indenter.[4–6] High-pressure experiments and nanoindentation studies have consistently shown that cubic Si (dc-Si) transforms to a denser, metallic β-Sn phase at roughly 11–12 GPa.[7–10] Upon unloading, the β-Sn phase does not revert to diamond cubic; instead, it decompresses into metastable forms. Slow unloading favors crystalline R8/BC8 phases, whereas rapid unloading quenches the structure into amorphous silicon (a-Si).[8,11,12] These transformations are evident in nanoindentation load, P – displacement, h curves as sudden "pop-in" events (dc-Si → β-Sn) and "pop-out" events (β-Sn → R8/BC8), whose pressure signatures correlate well with bulk transition pressures.[13–15] For example, Juliano *et al.* found that under slow unloading and high loads, pop-out events (indicative of R8/BC8 formation) became more frequent, whereas fast unloading produced predominantly amorphous material.[5,16,17] In short, silicon's nanoscale mechanical response is dominated by pressure-driven phase changes, whose occurrence and products depend sensitively on the applied load and unloading rate.[13,18]

The geometry of the indenter strongly affects the stress state beneath the contact, and thus the resulting phase distribution and fracture behavior.[19] Sharp (Berkovich) indenters create a highly concentrated stress field under the tip, whereas spherical indenters distribute hydrostatic pressure over a larger zone.[16,19,20] As a result, spherical contacts generally require higher loads to reach the same peak pressure and tend to generate a larger volume of transformed material. Juliano *et al.*[5] observed that both Berkovich and spherical indenters exhibit higher β-Sn → R8/BC8 transformation pressures at higher peak loads, but a larger spherical tip radius necessitates a greater load for equivalent transformation, due to its blunter contact. Crucially, Zarudi *et al.*[21] directly compared cross-sectional electron microscopic images of Berkovich and spherical indents (cross-sectional Transmission Electron Microscopy (XTEM)) and found markedly different phase distributions. Under Berkovich loading, the highest hydrostatic stress occurs right at the indenter tip, so that crystalline R8/

[a]*Department of Physics and Nanotechnology, SRM Institute of Science and Technology, Kattankulathur-603203, Tamil Nadu, India. E-mail: ms8267@srmist.edu.in*
[b]*Centre for Interdisciplinary Research, SRM University-AP, Amaravati, Andhra Pradesh 522240, India. E-mail: kiran.k@srmap.edu.in*

BC8 phases form deep at the bottom of the transformed zone. By contrast, spherical indenters concentrate hydrostatic stress in the upper part of the contact, producing R8/BC8 phases nearer the surface of the plastic zone.[22] Molecular-dynamics and finite-element simulations corroborate this: Berkovich tips yield peak hydrostatic pressure beneath the apex (favoring deep transformations), whereas spheres peak shallower (favoring near-surface crystallization).[18,21,23,24]

These stress differences also influence fracture. Sharp indenters induce strong shear stresses near the contact edges, often leading to well-known radial and median cracks.[25] Indeed, median cracks emanating from the base of the transformed zone are commonly seen under pyramidal tips.[26,27] In contrast, spherical indenters tend to produce laterally oriented or ring-shaped cracks at larger indentation depths, since the plastic zone is more uniform and subsurface. In practice, nanoindentation of Si with sharp tips frequently shows surface radial cracks at diagonal corners, whereas spherical loading produces broader transformation zones with fewer early surface cracks.[6,28] Juliano *et al.* and others report that all indenter types eventually generate cracks once the transformation zone grows large, but the sharp *vs.* blunt geometry dictates where and when they form.[5] Therefore, the geometry of the indenter influences the stress fields and affects the balance between phase transformation and brittle fracture in silicon. The molecular dynamics study shows crack-driven brittle deformation in silicon during nanoindentation, providing the first successful MD prediction of median cracking in Si under large indentation strains,[15] while McMahon *et al.* showed pressure-induced phase stability windows for various Si polymorphs, laying the foundation for understanding atomistic mechanisms of damage evolution in crystalline Si.[29]

Oxide-capped silicon (SiO_2/Si) structures are widely used in CMOS, MEMS, and photonic devices, where mechanical reliability under localized contact stress is essential. Thin SiO_2 layers function as gate dielectrics, passivation layers, or insulators, and mechanical failure in these films can degrade or destroy device functionality. In real devices and processing, silicon is rarely uncoated; a common case is thermal SiO_2 on Si.[30] The oxide layer introduces additional mechanical constraints and failure pathways. Thermally grown SiO_2 is a brittle, low-toughness film (fracture toughness $\ll$1 MPa $m^{0.5}$), while the Si substrate is much stiffer.[30,31] Under indentation, the amorphous SiO_2 can deform by densification and shear of the Si–O network, but it also tends to crack if stresses are high. For example, MD simulations show that SiO_2 will densify and stretch under load, but if loading is too rapid, the film fractures rather than densifying. In Chen *et al.*'s MD study, higher indentation rates caused the 20 nm SiO_2 cap to crack early, leading to larger shear stresses in the silicon and a shift toward crystalline-to-amorphous transformation in the Si.[32] Conversely, thicker or more compliant oxide layers can delay silicon's phase change. Another MD study found that thinner SiO_2 films allowed the dc-Si → β-Sn transformation to occur at shallower depths, so that more atoms underwent transformation at a given indentation depth.[33] In effect, a stiff oxide coating supports the silicon and raises the effective transformation pressure, whereas if the oxide breaks, the silicon relaxes more freely.

Coatings also influence cracking. In layered systems, indentation can produce ring-shaped cracks in the film or interface delamination, depending on relative stiffness and adhesion.[34] For instance, Ke *et al.* observed that a brittle MoS_2 film on SiO_2 delaminated and cracked in a circular pattern under indentation, whereas a more compliant graphene film did not.[35] By analogy, indentation of SiO_2/Si may produce circular (ring) cracks in the oxide and/or median cracks in the Si substrate. In practice, the strongly bonded thermal oxide may crack through-thickness (*e.g.* lateral cracks) under high tensile stress or allow tensile energy to drive cracks into the silicon. To date, there are few direct studies of indentation-induced cracking in SiO_2/Si systems. Most nanoindentation of oxide films focuses on extracting hardness and modulus by accounting for substrate effects,[36,37] and studies of film delamination typically involve cross-section techniques. The net effect is that the oxide coating modifies both the stress distribution and the failure mechanisms altering the onset and pattern of cracks relative to bare Si, but a systematic experimental picture is lacking.

Despite the extensive literature on silicon indentation and separate work on film–substrate mechanics, the combined problem of phase transformation *versus* fracture in oxide-coated silicon remains poorly understood. In particular, it is not known how a thermal SiO_2 cap alters the competition between pressure-induced phase changes and crack formation under different indenter geometries. Existing studies have either treated uncoated Si (examining pop-in/pop-out and crack initiation) or have simulated coated systems (revealing trends in oxide thickness and rate effects).[33] What is missing is a direct experimental comparison of sharp *versus* blunt indentation on the same SiO_2/Si(100) system, tracking where and how phases and cracks emerge. How does the oxide constraint change the pressure needed for β-Sn formation or the likelihood of pop-out events? Does a Berkovich tip trigger oxide-confined crack pattern different from those under a spherical tip? Answering these questions is important for semiconductor and MEMS reliability, as mechanical contacts in devices can inadvertently drive unwanted transformations or fractures.[33] For example, phase-transformed silicon has altered density and electrical properties, which could disrupt device function, and oxide cracks can provide pathways for contamination or device failure.

To fill these gaps, we perform a systematic comparison of indentation-induced phase transformations and cracking in SiO_2/Si(100) under both Berkovich and spherical loading. Using micro-Raman spectroscopy and high-resolution imaging of the residual impressions, we correlate the occurrence of R8/BC8 or amorphous Si with the crack morphology, without resorting to post-indent annealing or pre-imposed models.[38] In contrast to prior reports, no annealing is used, so all measured phases are those immediately formed by the indentation. To our knowledge, this is the first study to directly

compare sharp *vs.* blunt indenters on thermally oxidized Si, revealing how the oxide layer shifts the balance between pressure-driven polymorphism and fracture. Such insights are novel and timely for understanding contact damage in Si-based microelectronic and nanomechanical systems, where the SiO_2 layer and contact geometry jointly govern mechanical reliability.

2. Experimental

Nanoindentation was employed as the primary technique to investigate phase transformation behavior in silicon with a deposited SiO_2 surface layer. The samples consisted of boron-doped p-type Czochralski-grown Si(100) wafers with a resistivity of approximately 10 Ω cm. These wafers, coated with a ~285 nm thick SiO_2 layer, were procured from a commercial supplier in 1×1 cm^2 dimensions. The oxide film served as a mechanical constraint layer, allowing systematic investigation of its effect on the pressure-induced phase transformations occurring in the underlying silicon substrate.

All indentation experiments were carried out at room temperature using a NIOS Advanced Nanohardness Tester (Ostec Instruments, Russia), which has a maximum load capacity of 1.25 N. Two different indenter geometries were used: a Berkovich diamond tip and a spherical sapphire tip with a radius of 20 μm. The comparative use of these two geometries enabled controlled variation in stress distribution: the Berkovich tip, expecting a sharp, highly localized stress field, while the spherical tip generates a more distributed and quasi-hydrostatic pressure field.

For spherical indentation, loads were systematically varied from 80 mN up to 500 mN. Each indentation cycle included a 30-second loading segment, a 10-second holding period at peak load, and a 30-second unloading segment. Similarly, Berkovich indentations were conducted at a range of loads from 20 mN to 500 mN.

Complete *P*–*h* curves for all tested loads are presented in SI as Fig. S1, with a minimum of three overlaid replicates per condition to assess reproducibility. Curves are explicitly annotated with pop-in occurrence (loading), pop-out events (unloading, marked by displacement plateaus), peak displacement (h_{max}), and residual displacement ($h_{residual}$). These mechanical signatures are then correlated with post-indentation Raman and cross-sectional TEM analysis to link mechanical events (pop-in/pop-out) to underlying structural transformations (R8/BC8 formation). Reproducibility across replicates is excellent: standard deviations in h_{max} and $h_{residual}$ are typically 1–2% of mean values, and pop-out loads show coefficients of variation (SD/mean) of 2–19%, confirming consistent mechanical response. Variability increases at high loads or in conditions with probabilistic pop-out occurrence, consistent with nucleation-limited phase transformation behavior.

Micro-Raman spectroscopy was used to probe the phase composition of the residual indent zones. Spectra were collected using a Horiba LABRAM HR Evolution Raman spectrometer equipped with a 633 nm HeNe laser. A 100× objective lens was used to focus the laser beam to a spot size of approximately 1 μm. The laser power was restricted to 18 mW to avoid any local heating or inadvertent annealing of metastable phases. Raman spectra were acquired from both Berkovich and spherical indents at various loads. The optical microscopic images were obtained from the microscope attached to Raman system.

High-resolution Scanning Electron Microscopy (SEM) images were obtained using a Thermo Scientific Apreo system to capture the residual impressions left by spherical and Berkovich indentations under various loads. These images reveal distinct deformation signatures for each indenter geometry, confirming their size and surface morphology. The SEM imaging provided valuable insights into the deformation zone, including aspects such as radial cracking, pile-up, and delamination around the indents. This information complements the mechanical data obtained from the load–depth curves.

For detailed subsurface analysis, cross-sectional lamellae were prepared using a FEI Helios 600 NanoLab dual-beam focused ion beam (FIB) system. A protective platinum layer was deposited *via* electron beam over the targeted indent region to preserve the surface integrity during milling. Bright-field TEM imaging and selected area electron diffraction (SAED) analyses were carried out on a Philips CM300 instrument operating at 300 kV. Care was taken in interpreting SAED patterns due to overlapping *d*-spacings among high-pressure silicon polymorphs; each diffraction spot was carefully assigned based on orientation, zone axis alignment, and literature-reported interplanar spacings.

3. Results

3.1 Nanoindentation

Fig. 1 compares representative nanoindentation *P*–*h* curves for 285 nm SiO_2/Si(100) under a Berkovich indenter (Fig. 1a and b) and a spherical indenter (Fig. 1c and d). The Berkovich *P*–*h* curves exhibit the expected elastic–plastic response with a sharp initial loading slope followed by yielding. Notably, upon unloading from sufficiently high loads, a sudden displacement burst or "pop-out" event is observed in the Berkovich curves (manifested as a horizontal plateau/drop in load).[4,39] The first pop-out occurs at a critical load of approximately $P \approx 42$ mN for Berkovich indents, indicating the detectable formation of a pressure-induced phase transformation during unloading. At peak loads just above this threshold, typically a single pop-out is seen, whereas multiple or stepped pop-outs can appear at higher loads as the transformed volume grows.[2,5] For example, indentations up to 100 mN often show an initial pop-out around ~40–45 mN on unloading, and occasionally a second smaller pop-out at lower loads as residual high-pressure phases continue to transform. The pop-out corresponds to a sudden increase in indent depth (on unloading) by tens of nanometers, evidencing the formation of lower-density phases

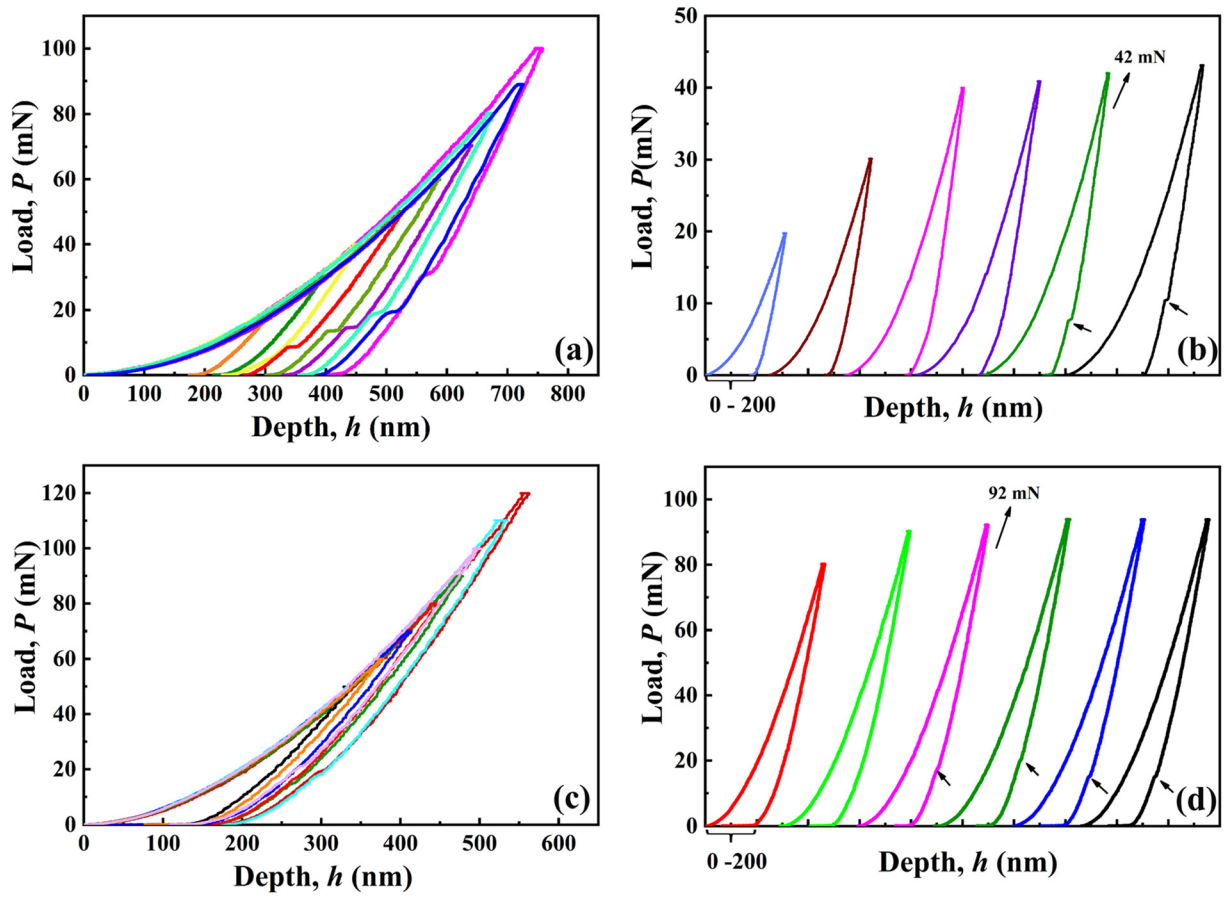

Fig. 1 Load–displacement curves for nanoindentation on SiO_2/Si(100) using Berkovich and spherical indenters. (a) Representative *P*–*h* curves from Berkovich indentation at various peak loads (20–100 mN), showing continuous elastic–plastic response with increasing depth. (b) Magnified view of Berkovich indentations recorded at selected peak loads(20, 30, and closely spaced loads between 40 and 45 mN), highlighting the onset of pop-out events (marked by arrows), first observed at ~42 mN, indicating formation of sufficient volume of pressure-induced phase transformations in the silicon substrate. (c) *P*–*h* curves from spherical indentation (50–120 mN), showing more gradual penetration due to the distributed contact stress field. (d) Enlarged view of spherical indentation curves obtained at selected peak loads (80, 90, and closely spaced loads between 90 and 95 mN) demonstrating delayed pop-out onset (~92 mN), corresponding to transformation-induced volume recovery in the phase-transformed zone. The contrast between Berkovich and spherical geometries underscores the geometry-dependent nature of stress distribution, phase transformation kinetics, and mechanical instability in oxide-coated silicon.

(compared to β-Sn phase) that expand the material and push the indenter upward.[4] Quantitatively, the Berkovich indents reach ~600 nm depth at 90 mN load (Fig. 1a), and the unloading stiffness is high, consistent with significant elastic recovery, until the pop-out event causes a discrete jump in depth. However, it is important to note that the absence of a noticeable pop-out event does not necessarily imply the absence of phase transformation. As noted in prior studies, pop-outs may be suppressed or rendered undetectable when the transformed volume is extremely small, the unloading rate is fast, or the resolution of the displacement detection is limited.[18,40] Thus, phase transformations may still occur in sub-critical volumes without causing a measurable discontinuity in the unloading curve.

By contrast, the spherical indenter (radius ~20 μm) produces a markedly different *P*–*h* response (Fig. 1c & d). The loading curve for the spherical tests is initially purely elastic and smoothly transitions into an elastic–plastic regime without the sharp knee observed for Berkovich. In some cases, a subtle "pop-in" (sudden depth excursion) occurs on the spherical loading curve at ~40 mN, corresponding to the yield point where the Si first undergoes a phase transformation (dc-Si to high-pressure β-Sn) beneath the indenter.[20] However, plastic deformation in spherical indentation is more gradual, owing to the distributed contact area. The spherical indentations can sustain much higher loads before any discontinuity: a clear pop-out on unloading is not typically seen until $P \approx$ 92 mN, more than double the Berkovich critical load.[20] Once this ~92 mN threshold is exceeded, an unloading pop-out event occurs analogously to the Berkovich case, but with a larger associated depth recovery, reflecting the larger transformed volume under the spherical indenter. The *P*–*h* curves for spherical indents show higher elastic loading stiffness and shallower penetration at a given load (*e.g.* at 100 mN, $h \approx$

300 nm for spherical *vs.* $h \approx 500$ nm for Berkovich), consistent with the lower mean contact pressure of the blunt indenter. Importantly, all observed mechanical responses, including elastic–plastic transition, depth recovery, and phase transformation, are modulated by the presence of the oxide cap, which constrains the initial contact, alters subsurface stress profiles, and governs delamination thresholds. After the pop-out, the unloading slope of the spherical curve remains steep, indicating that significant elastic residual contact area persists. Hence, the Berkovich indenter produces pop-out events at lower loads (~42 mN) with smaller displacement bursts, whereas the spherical indenter delays the pop-out to ~92 mN but then exhibits a more pronounced depth recovery. These results highlight the influence of indenter geometry on the mechanical response: the sharper Berkovich induces earlier instability due to the highly concentrated stress field, while the spherical tip requires a larger load to reach the same critical pressure under the more distributed contact.[21,26]

3.2 Raman analysis

Post-indentation Raman micro-spectroscopy confirms that the pop-out events coincide with pressure-induced phase transformations in the Si substrate. As shown in Fig. 2, Raman spectra collected from within Berkovich indent impressions (at various peak loads) reveal the emergence of new peaks at approximately 165, 353, 381, 399 and 443 cm^{-1}, alongside the characteristic 520 cm^{-1} band of crystalline Si. These peaks correspond to the vibrational modes of metastable high-pressure polymorphs of silicon: specifically, the bands in the ~350–440 cm^{-1} range are attributable to the R8 and BC8 phases.[41–43] A low-frequency shoulder near 165 cm^{-1} is also observed, which has been assigned in literature to R8.[43] For Berkovich indents just above the 42 mN threshold (where a single small pop-out occurs), the R8/BC8 peaks are present but weak, indicating a modest volume of transformed material. At higher loads (*e.g.* 100 mN and above, where larger pop-outs were seen), the R8/BC8 Raman peaks become much more pronounced, and in some cases, multiple peaks (*e.g.* at ~384 cm^{-1}, 353 cm^{-1}, ~399 cm^{-1}, and ~443 cm^{-1}) are resolved, suggesting a mixture of R8/BC8 phases.[41,43,44] Concurrently, the intensity of the original 520 cm^{-1} dc-Si peak diminishes for large indents, consistent with a significant portion of the probed volume no longer being in the diamond-cubic phase. We also note that certain Berkovich indents (especially those made with rapid unloading or just below the pop-out load) yielded a broad hump around 480–500 cm^{-1} in the Raman spectrum. This broad band is characteristic of amorphous silicon (a-Si),[45,46] indicating that a fraction of the transformed zone had vitrified instead of crystallizing. In general, however, whenever a pop-out was observed in the Berkovich tests, the post-indentation Raman spectra showed sharp peaks of R8/BC8, implying that the pop-out event corresponds to the formation of these crystalline polymorphs during unloading.

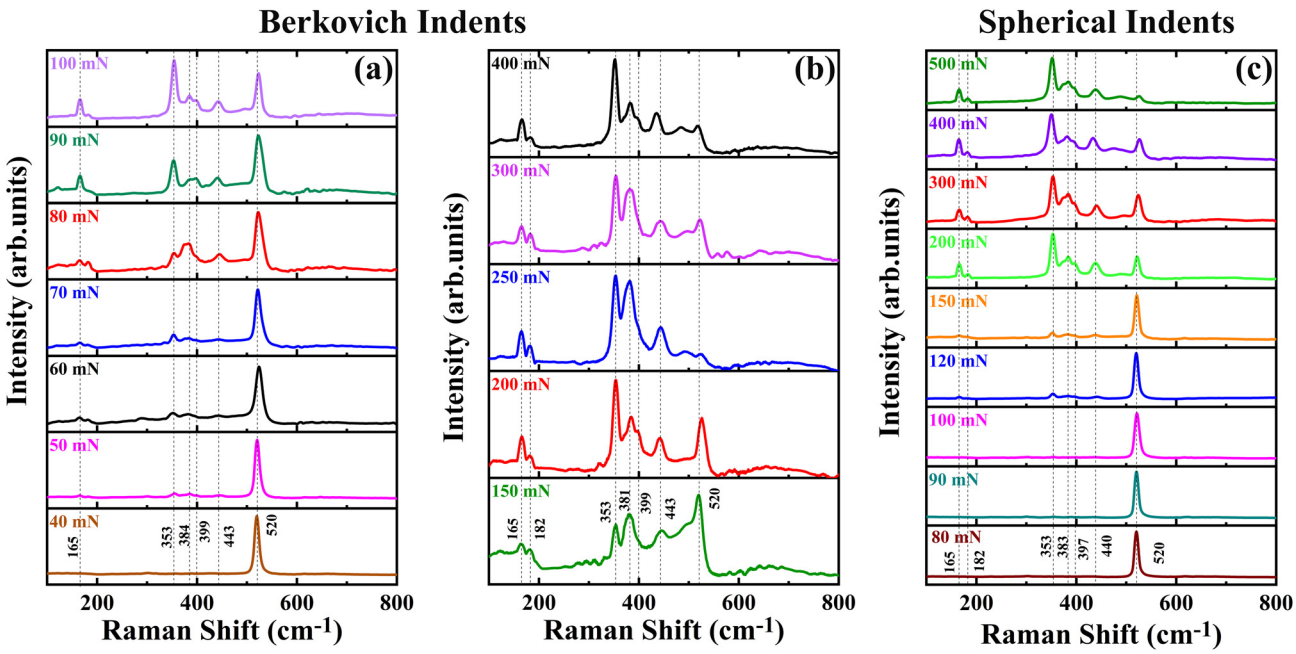

Fig. 2 Raman spectra obtained from residual indents on 285 nm SiO_2/Si(100) using Berkovich and spherical indenters. (a and b) Raman spectra from Berkovich indents at increasing loads (40–100 mN and 150–400 mN, respectively) showing the emergence and intensification of peaks at ~165, 353, 381, 399, and 443 cm^{-1}, corresponding to high-pressure crystalline phases R8 and BC8, alongside the diminishing intensity of the diamond cubic Si peak at 520 cm^{-1}. (c) Raman spectra from spherical indents at loads ranging from 80 mN to 500 mN, displaying a similar evolution of metastable phase signatures, with delayed onset of transformation features compared to Berkovich indentation. The load-dependent appearance of R8/BC8 peaks and reduction in the 520 cm^{-1} band confirm pressure-induced polymorphism in the substrate, with geometry-dependent differences in transformation volume and phase distribution.

Spherical indentations exhibited a load-dependent phase transformation signature in Raman spectra that complements the Berkovich results. At sub-critical loads (*e.g.* 80 mN, where no pop-out occurred), the Raman spectrum under the spherical indent is dominated by the 520 cm^{-1} crystalline Si peak with only a very weak amorphous signature and no obvious R8/BC8 peaks. This suggests that when the spherical indenter does not induce a pop-out (*i.e.* the critical pressure is not reached to form β-Sn phase during loading), the residual affected zone is primarily a mixture of amorphous Si and unreverted dc-Si. Once the spherical indentation exceeds ~92 mN (*i.e.* sufficient threshold transformation pressure) and a pop-out takes place, clear R8/BC8 peaks appear in the Raman spectra, mirroring the Berkovich case. For instance, spherical indents driven to 120 mN show the emergence of distinct peaks near 165 cm^{-1}, 353 cm^{-1}, 381 cm^{-1}, and 440 cm^{-1}, superimposed on a still-dominant dc-Si band. At higher loads (200–500 mN), these metastable phase peaks become progressively more intense and sharper, indicating growth of the crystalline high-pressure phase regions.[41] Concurrently, the amorphous contribution associated with the 480 cm^{-1} band remains detectable at higher loads, even though the larger transformed volume is generally more prone to crystallize during unloading. These observations are in line with prior reports that the formation of R8/BC8 is favored by higher indentation loads and slower unload rates.[47,48] Hence, Raman analysis confirms that both indenter geometries induce the same types of phase transformation in silicon, formation of β-Sn during loading, which upon unloading either amorphizes or transforms to R8/BC8, but the onset and extent of these transformations depend strongly on indenter geometry and load. The Berkovich tip triggers phase changes at lower loads (consistent with the early pop-outs), whereas the spherical indenter requires higher loads to activate the phase transformation (hence delayed Raman signature of R8/BC8). Notably, once the transformation is activated, the spherical indentation can produce a larger volume of transformed (metastable) Si, as evidenced by the strong Raman signals at higher loads.

3.3 Cross-sectional SEM analysis

Post-indentation optical and electron microscopy reveal distinct deformation and fracture patterns for Berkovich *vs.* spherical indentations. Fig. S2 in the SI shows optical micrographs of a series of Berkovich indents at increasing loads. At low loads (just above the elastic limit, *e.g.* 20–30 mN), the Berkovich impressions are barely visible; only a faint triangular contact area can be seen with no cracking or delamination in the oxide. Once the load reaches the pop-out threshold (~42 mN), small radial cracks begin to emanate from the three corners of the triangular indent.[49] These cracks appear as straight or slightly curved dark lines extending outward by a few microns from each indent corner in optical images. Concomitantly, interference colors become apparent around the indent perimeter, manifesting as concentric rings or patches of pink/green tint (Fig. S2, middle frames). The appearance of these color fringes indicates the SiO_2 film has delaminated or lifted slightly, creating an air gap that produces optical interference, essentially evidence of the oxide film debonding due to the substrate deformation. With further increasing load, the cracking and delamination become more pronounced. High-load Berkovich indents (*e.g.* 100 mN and above) exhibit a network of radial and lateral cracks and extensive film fragmentation. In optical images (Fig. S2, bottom frames), the indent sites are surrounded by jagged, colorful regions where the oxide has buckled or flaked off. The triangular imprint itself often shows edge "pile-up", the edges of the indent appear elevated, which is actually the detached oxide film bent upward rather than true plastic pile-up of substrate material. Around these heavy indents, we observed lateral cracks running roughly parallel to the surface, which led to partial spallation of both the oxide and underlying silicon.[50] Chipping of the film is evident as bright reflective shards around the indent. Scanning electron microscopy of a 100 mN Berkovich indent confirms these features in greater detail: a roughly triangular crater is present in the Si, and the surrounding oxide film is extensively cracked and delaminated. The SEM image shows pieces of the SiO_2 film that have been completely detached and tilted up around the indent, as well as a debris field of smaller fragments. Beneath some of these film fragments, one can see the exposed silicon substrate. There is minimal continuous material pile-up at the indent edges; instead, the imprint is bordered by a rough, irregular raised rim corresponding to the fragmented film. These observations indicate that the Berkovich indentation induced severe brittle fracture in the coating and substrate: a classic radial-median crack system in the silicon (the median crack subsequently intersecting the surface as radial cracks coupled with film decohesion and lateral cracking that removed material). The presence of lateral cracks (horizontal cracks roughly at the film/substrate interface) is supported by the fact that entire portions of the oxide have been cleanly sheared off and pushed outward (a result of a lateral crack propagating and lifting the surface layer). In several cases we noted that the silicon substrate itself had chipped: tiny silicon pieces were pried out alongside the oxide, consistent with the formation of Hertzian cone cracks or substrate lateral cracks at high load.[50]

Spherical indentations produce a different post-indentation morphology, reflecting the more distributed contact stresses, as shown in Fig. S3 in SI. At low to moderate loads (*e.g.*, 60–80 mN, below the pop-out threshold), spherical indents leave only subtle marks. The indent sites appear as very shallow circular depressions in the oxide; under optical microscope, they may show a faint Newton-ring pattern or a slight greyish dent, but no obvious cracks. The oxide film remains largely intact at these loads, indicating that the deformation was accommodated elastically or *via* phase transformation without reaching the film's fracture strain. Once the load exceeds ~92 mN and a pop-out/phase transformation occurs, however, distinctive fracture patterns emerge. Optical micrographs of spherical indents in the ~100–200 mN range show the development of concentric "ring" cracks in the oxide.[51] These appear as roughly circular or hexagonal cracks outlining

the perimeter of the contact area. Frequently, one or two ring cracks form just outside the indent contact edge, often accompanied by radial cracks that span between the rings (creating a star-like pattern emanating from the indent center). In some cases, the ring cracks lead to partial flaking of the oxide in an annular shape around the indent. The interference colors around spherical indents tend to be more symmetric (halo-like) compared to the tri-color lobes around Berkovich indents, again reflecting the circular symmetry of the stress field. At higher loads (300–500 mN), the extent of cracking in spherical indentation increases: multiple ring fractures can form, and radial cracks may extend further out, dividing the circumference into segments. SEM inspection of a 500 mN spherical indent reveals a roughly circular crushed zone about ~10 μm in diameter. The oxide film within this zone is extensively fractured and partially removed; however, unlike the Berkovich case, the central region exhibits a more continuous, depressed area rather than a deep triangular punch. The film fragments from the spherical indent are fewer and larger (often curved shell-like pieces corresponding to the ring crack outlines). We did not observe pronounced three-fold radial crack patterns for spherical indents; instead, any radial cracks were evenly distributed and often initiated at points along the ring cracks (sometimes due to pre-existing film defects). The substrate silicon under spherical indentation also experienced cracking at high loads, evidenced by some radial cracks propagating into the silicon (these can be inferred from straight crack lines crossing the remaining film).[27] However, the silicon cracks under spherical contacts tend to initiate later and in a more stable manner (no large chunks of silicon were dislodged at 500 mN, in contrast to the Berkovich case where substrate chipping occurred around 100 mN). Pile-up in spherical indents was minimal as well, but we did observe a subtle outward bulging of the oxide at the contact edge in some cases. This slight raised lip around the spherical impression likely stems from the volumetric expansion of the transformed silicon (R8/BC8 have lower density than the compressed β-Sn phase) and the bending of the oxide film.[33] Unlike a ductile metal, Si cannot flow freely, so this "pile-up" is actually the elastic rebound and film uplift rather than plastic extrusion of material.[52] Overall, the spherical indentation causes more delocalized damage: the energy goes into creating a broad transformed zone and eventually ring cracks, rather than the concentrated median crack and massive spallation seen with the sharp indenter. The oxide film, while ultimately cracking and delaminating at high loads, survives to higher contact pressures under spherical loading; when it does fail, it tends to come off in circumferential pieces.[34,37] These distinct residual imprint morphologies for Berkovich *vs.* spherical indents underscore the differing mechanical and fracture processes at play, as discussed below.

To probe the load-dependent deformation mechanisms and fracture evolution in the SiO_2/Si bilayer under different indenter geometries, cross-sectional scanning electron microscopy was performed on focused ion beam milled nanoindents created using both spherical and Berkovich tips at specific loads (Fig. 3). The images highlight the interplay between contact geometry, applied load, and the resulting stress field distribution, revealing insights into high-pressure phase transformation, crack formation, and oxide delamination.

At 200 mN (Fig. 3a), the spherical indent induces a shallow, hemispherical deformation zone with distinct dark contrast indicative of a high-pressure phase transformation to R8/BC8 silicon. This transformed zone lies beneath the 285 nm SiO_2 overlayer and is confined without any visible crack initiation. The absence of median or lateral cracks suggests that under near-hydrostatic conditions, the spherical tip favors phase transformation over brittle fracture at moderate loads.[53] The oxide layer remains fully intact, offering slight constraint without damage propagation. At 500 mN (Fig. 3b), the extent of deformation increases substantially. A significantly enlarged R8/BC8 region is observed beneath the indent, indicating an expanded transformation volume at elevated load. Notably, this is accompanied by the development of severe cracking: a dominant median crack propagates vertically into the crystalline silicon substrate, while lateral cracks emanate outward along the Si/SiO_2 interface. These cracks intersect to form a classic Y-shaped fracture morphology, characteristic of Hertzian cone fracture.[54] While the SiO_2 layer mostly retains its continuity, its slight distortion near the crack tips suggests localized delamination or decohesion under high tensile and shear stresses.

At 100 mN (Fig. 3c), the sharp Berkovich tip produces early-onset fracture features, even at lower loads. A prominent median crack initiates from the indent apex, and a long radial crack extends toward the substrate surface. Despite the relatively low applied load, the sharp indenter geometry creates localized stress concentrations that surpass the fracture toughness of silicon, leading to brittle failure.[39] A small R8/BC8 transformed region is still visible beneath the contact, but cracking dominates the deformation behavior. The SiO_2 film remains mostly adhered but shows signs of interfacial stress release near the cracks. At 500 mN (Fig. 3d), the subsurface damage is significantly more pronounced. The indentation leads to a dense, asymmetric R8/BC8 phase-transformed region surrounded by a complex fracture network comprising radial, median, and lateral cracks.[6,49] Importantly, the SiO_2 layer undergoes partial delamination, particularly at the edge of the indent where tensile stresses are amplified during unloading. The presence of through-thickness cracks and wrinkling in the oxide layer indicates interfacial decohesion and film buckling. The transformed region beneath the indent also shows variable thickness, highlighting the role of geometric and load asymmetry in stress redistribution.[33,55]

These results clearly demonstrate that both indenter geometry and applied load critically govern the subsurface deformation behavior in silicon with a thin oxide overlayer. While spherical indenters at moderate loads enable stable phase transformation without cracking, higher loads promote classical Hertzian fracture morphologies. In contrast, Berkovich indenters initiate cracking even at lower loads due to intense stress gradients, leading to extensive damage and oxide dela-

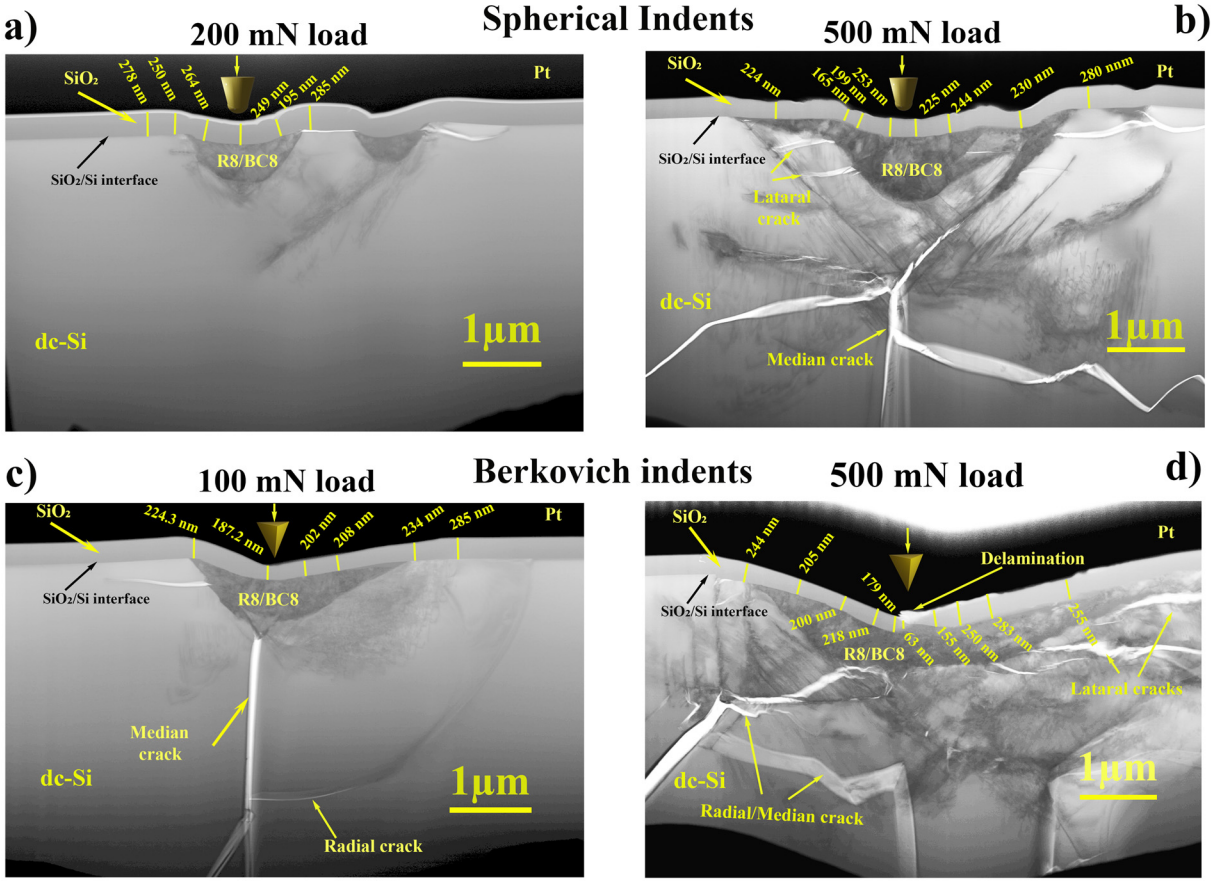

Fig. 3 Cross-sectional SEM images of FIB-milled nanoindents on (100) Si substrates coated with ~285 nm thermally grown SiO_2, showing load- and geometry-dependent subsurface deformation and fracture patterns. (a) Spherical indentation at 200 mN reveals a shallow, localized high-pressure R8/BC8 phase-transformed zone without observable cracking, suggesting plastic deformation and transformation-dominated behavior. (b) Spherical indentation at 500 mN shows an enlarged R8/BC8 region along with extensive subsurface damage, including lateral cracks parallel to the SiO_2/Si interface and a median crack propagating into the bulk, forming a Y-shaped fracture network. (c) Berkovich indentation at 100 mN exhibits early crack initiation, with a dominant median crack beneath the indent and a radial crack extending to the surface; the transformed R8/BC8 zone remains relatively confined. (d) Berkovich indentation at 500 mN reveals severe fracture, including multiple radial/median/lateral cracks and substantial delamination of the SiO_2 layer, which undergoes through-thickness cracking and buckling due to tensile stress. The damage morphology highlights the pronounced influence of indenter geometry and load on deformation behavior and interfacial integrity.

mination at higher loads.[19] The SiO_2 layer provides partial constraint and affects crack deflection paths but is unable to prevent fracture propagation when substrate failure occurs. These observations have critical implications for designing mechanically robust Si-based systems with surface oxide layers under contact stress environments.

3.4 Cross-sectional TEM analysis

To gain deeper insights into the subsurface structural transformations induced by nanoindentation, cross-sectional bright-field TEM, SAED pattern, and HRTEM were performed on FIB-milled lamellae prepared from Berkovich and spherical indents at various loads, as shown in Fig. 4[a–l].

The bright-field TEM image obtained from the Berkovich indentation at 100 mN load (Fig. 4a, e and i) reveals a localized, triangular high-pressure phase zone confined beneath the Berkovich indent tip, with clear morphological contrast from the surrounding crystalline dc-Si. The phase-transformed region spans across the SiO_2/Si interface, highlighting vertical stress transmission and interfacial accommodation. The corresponding SAED pattern (Fig. 4e) collected from the transformed zone shows diffuse diffraction rings with spacings of ~3.2 Å, 2.69 Å, and 2.52 Å, consistent with R8, confirming pressure-induced transformation from dc-Si.[56] The HRTEM image (Fig. 4i) resolves a distinct, sharp interface between the thermally grown SiO_2, the R8/BC8 region, and the underlying Si matrix, with minimal intermixing or defect pile-up. This suggests that at lower loads, the Berkovich tip is capable of initiating phase transformation with limited interfacial disruption.

Berkovich indentation at 500 mN load (Fig. 4b, f and j) shows significant changes in deformation morphology. The transformed R8/BC8 region appears much more extensive in the TEM image (Fig. 4b), forming a lens-like zone that spans

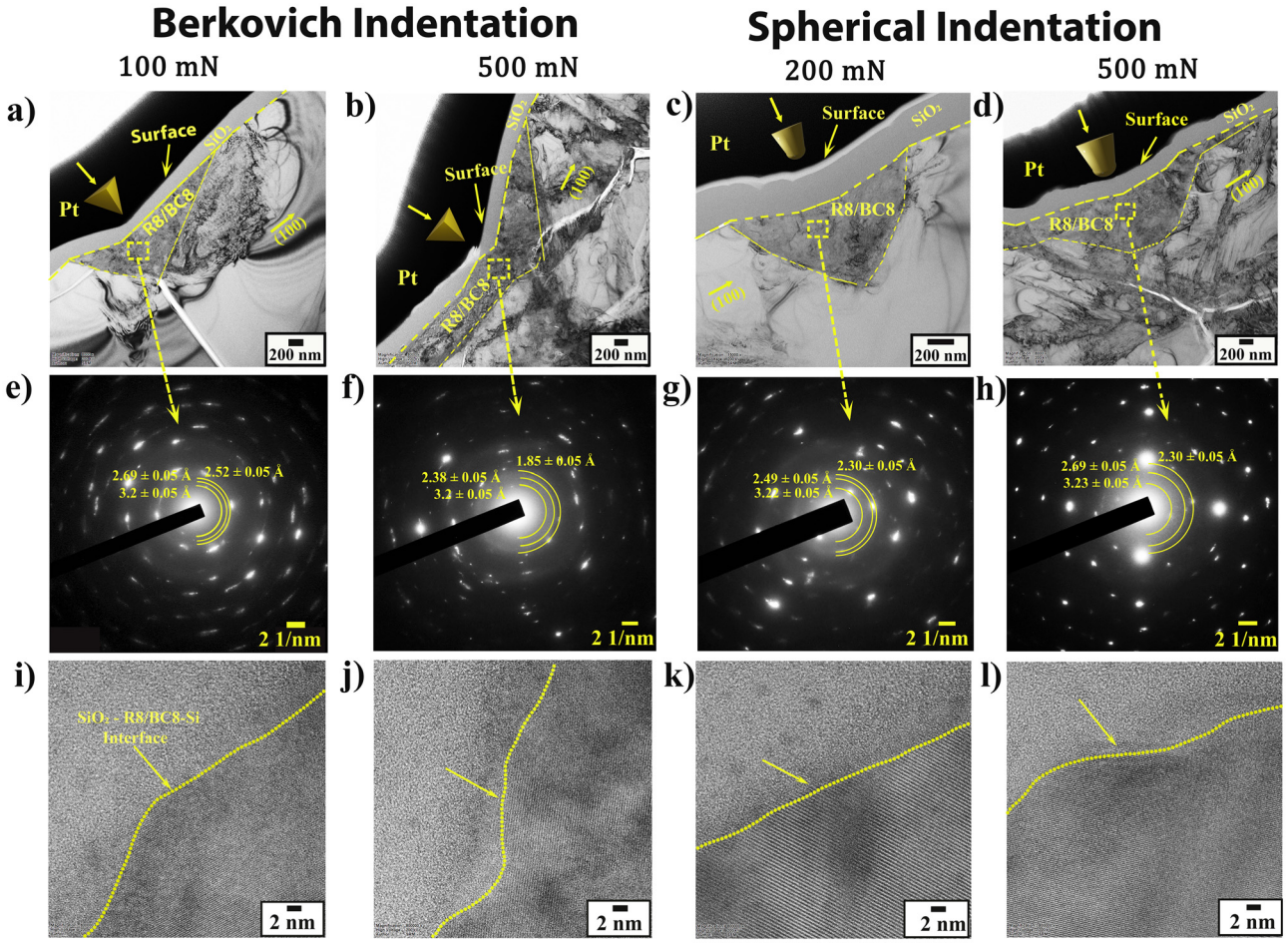

Fig. 4 Cross-sectional bright-field TEM analysis comparing the structural evolution beneath Berkovich and spherical nanoindents in Si(100) with a 285 nm thermally grown SiO_2 overlayer. (a–d) Low-magnification TEM micrographs showing the extent and morphology of the R8/BC8 phase-transformed regions under different loads: (a) Berkovich indent at 100 mN, (b) Berkovich indent at 500 mN, (c) spherical indent at 200 mN, and (d) spherical indent at 500 mN. The transformed regions are bounded by dashed lines and show geometry-dependent shape and interface interaction. (e–h) Corresponding SAED patterns confirm the formation of high-pressure R8/BC8 phases under all conditions, with additional diffuse rings or spot splitting at higher loads indicating strain or defect accumulation. (i–l) High-resolution TEM images taken across the SiO_2-R8/BC8interface for each condition show load- and geometry-dependent variations in interfacial coherence, crystallinity, and lattice distortion. Spherical indentation preserves relatively smoother and coherent interfaces, while Berkovich indentation leads to increased interfacial roughness and local disruption at higher loads.

deeper and wider into the substrate. SAED (Fig. 4f) reveals additional ring splitting and peak broadening, with *d*-spacings of 1.85 Å, 2.38 Å, and 3.2 Å, signatures of phase heterogeneity and possibly strain gradients within the transformed region.[56–58] The HRTEM image (Fig. 4j) shows a roughened and partially disordered interface, indicating interfacial stress build-up and possible localized delamination. These features reflect severe plastic deformation, lattice bending, and enhanced defect generation at high stress concentrations under a sharp indenter.

Spherical indentation at 200 mN load (Fig. 4c, g and k): TEM micrograph (Fig. 4c) shows a more symmetric and dome-shaped transformed region below the indent with smooth boundaries, suggesting uniform stress distribution and hydrostatic compression. The SAED pattern (Fig. 4g) confirms the presence of high-pressure R8/BC8 phases with characteristic *d*-spacings of ~2.30 Å, 2.49 Å, and 3.22 Å. The ring sharpness indicates better crystallinity and reduced lattice strain compared to the Berkovich indent. HRTEM (Fig. 4k) shows a coherent and continuous interface between the R8/BC8 region and surrounding Si, with well-aligned lattice fringes and no signs of cracking or delamination. These findings suggest that spherical indentation at moderate load induces stable phase transformation with minimal damage.

Spherical indentation at 500 mN load (Fig. 4d, h and l): the spherical indent leads to a broader and deeper transformed zone (Fig. 4d), yet the shape remains smooth and symmetric without the pronounced shear-induced asymmetry seen in sharp indenters. SAED pattern (Fig. 4h) exhibits intense rings at ~2.3 Å, 2.69 Å, and 3.23 Å, again confirming extensive formation of R8/BC8 phases with relatively good crystallinity. See SI Table S1 for indexed *d*-spacings and phase attribution for

SAED patterns. The HRTEM image (Fig. 4l) shows a relatively intact interface with only mild undulations, indicating that even at high loads, spherical indentation promotes gradual and stable transformation rather than abrupt fracture or delamination.[59] The oxide layer remains well adhered to the transformed zone.

The cross-sectional TEM analysis reveals distinct differences in deformation mechanisms and interface behavior as a function of indenter geometry and applied load. Under Berkovich indentation, the transformed R8/BC8 phase region exhibits pronounced asymmetry and sharp boundaries, with increasing load leading to deeper penetration, higher strain gradients, and interfacial disruption. At 500 mN, the interface becomes visibly rough and disordered, indicating stress-induced delamination or defect accumulation.[60] In contrast, spherical indentation results in a more symmetric and dome-like phase-transformed region that expands uniformly with increasing load, preserving structural coherence. The SAED patterns consistently confirm the formation of mixed R8 and BC8 phases, but sharper and more defined diffraction rings under spherical loading suggest superior crystallinity and reduced strain.[17,61] HRTEM imaging further highlights the geometry-driven contrast in interface quality: while Berkovich indents induce noticeable interfacial roughening and possible mismatch, spherical indents retain well-aligned lattice continuity even at high loads. These results underscore the critical role of contact geometry in governing not only the extent and nature of phase transformation in silicon but also the mechanical stability and structural integrity of the SiO_2/Si interface under extreme conditions.

3.5 Quantitative statistical comparison: oxide-capped *vs.* bare Si

Table 1 shows the experimental parameters and the phase transition loads observed for the silicon dioxide on silicon system. Comparing these results with published data for bare silicon helps evaluate how the oxide cap shields and confines the material. This comparison shows how the dielectric layer changes the mechanical thresholds for the dc-Si to β-Sn–Si transition and affects the recovery of metastable phases.

The first critical observation is that oxide presence delays pop-out loads by a small but distinct margin.[5,22] This delay reflects the oxide's role as a lateral stress constraint: the SiO_2 cap resists lateral expansion of the silicon substrate during loading, slightly postponing the release of stored elastic energy that manifests as pop-out during unloading.[31,33] However, this effect is kinetic rather than thermodynamic. The mean contact pressures at pop-out (Table 1) are 25.6 GPa for oxide-capped Si (Berkovich, 100 mN) *versus* 24–26 GPa for bare Si reported in the literature,[5,21] a negligible difference within the experimental uncertainty (±10%). This equivalence indicates that the oxide does not measurably increase the phase-transformation pressure; instead, it slightly delays the kinetic pathway to transformation through geometric constraint.

For spherical indentation, the oxide effect is similarly modest: pop-out onset at 92 mN (this work) *versus* 80–85 mN (literature bare Si),[21,28] representing a ~7–10% increase. This smaller relative effect under blunt geometry likely reflects the distributed nature of spherical contact: the broader contact area means the oxide's constraining effect is more diffuse, and the more hydrostatic stress state of a sphere inherently suppresses geometric effects that amplify in Berkovich contacts. The spherical/Berkovich pop-out load ratio in our system is 92/42 = 2.19, closely matching the ratio predicted for bare silicon (80/35 ≈ 2.3), confirming that oxide presence does not fundamentally alter the geometry-dependent scaling of transformation thresholds. This remarkable consistency validates our sample preparation and methodology and supports the interpretation that oxide effects are perturbative rather than transformative.

A second key finding emerges when comparing indentation depths and residual impressions under Berkovich loading at 100 mN. In our oxide-capped system, we observe a maximum indentation depth (h_{max}) of 761 ± 4 nm and a residual depth ($h_{residual}$) of 399 ± 12 nm. Reported bare-silicon data at comparable loads show similar maximum depths but systematically

Table 1 Comprehensive statistical comparison of nanoindentation-induced phase transformations in 285 nm thermally grown SiO_2-capped Si(100)

System/ indenter	P (mN)	n	Pop-out (%)	Pop-out load (mN) ± SD	h_{max} (nm) ± SD	h_{res} (nm) ± SD	Mean/ peak pressure (GPa)	Transform depth (nm)	I_{353}/I_{441}	Phase dominance	Fracture mode
Berkovich	50	20	60	7.17 ± 1.26	527 ± 10	231 ± 16	38.3	296	1.32	R8 + BC8 mixed	Small radial cracks
	70	20	75	10.6 ± 1.4	638 ± 7.2	334 ± 15	25.5	303.5	1.52	R8 dominant	Extensive cracks
	100	20	100	14.3 ± 1.5	761 ± 4	399 ± 12	25.6	362.5	3.36	R8 dominant	Severe lateral + spall
	200	20	100	39 ± 13	1107 ± 4	585 ± 12	23.9	522	2.22	R8 dominant	Extensive delam.
	500	20	100	206 ± 11.5	1892 ± 24	1005 ± 18	20.2	887.3	—	—	Complete delam.
Spherical (R = 20 μm)	100	20	30	19.3 ± 3	503 ± 2	171.6 ± 6	11.1	331.4	1.07	R8 + BC8 mixed	Ring cracks
	150	20	90	25 ± 8.2	646.6 ± 7	207.6 ± 7	12.7	439	1.30	R8 + BC8 mixed	Multiple rings
	200	20	100	30 ± 17	769.6 ± 3	241.6 ± 3	14.0	528	2.43	R8 dominant	Ring + radial
	300	20	100	88 ± 6	1006.3 ± 7	344.3 ± 5	16.1	662	2.56	R8 dominant	Ring + cone
	500	20	100	167 ± 15.5	1373 ± 21	479.3 ± 8	19.0	893.7	3.06	R8 dominant	Annular delam.

See SI for calculation methodology and criteria for phase classification, pop-out detection, and contact mechanics.

smaller residual depths, indicating less permanent, transformation-driven deformation at the same load.[5,21,22,27,40] The disproportionately larger residual depth in the oxide-capped sample, which reflects the volume of irreversible deformation and phase transformation, suggests that the oxide layer modifies stress redistribution during indentation. By constraining lateral stress relaxation, the oxide promotes a more confined, depth-extended transformed zone beneath the indenter rather than lateral spread. This result supports the interpretation that oxide confinement alters local transformation mechanics and geometry, while the underlying pressure thresholds and phase-selection pathways in silicon remain essentially unchanged within experimental uncertainty.

Estimated transformed zone depths, evaluated as h_{max}–$h_{residual}$, are 362 nm for the oxide-capped sample, which is comparable to but slightly above the lower end of reported values for bare Si at similar loads. Using a simple conical approximation, this corresponds to a transformed volume of about 7.3 μm^3, lying near the upper end of the 6–8 μm^3 range reported for bare Si under Berkovich indentation by Zarudi *et al.*[21] These comparisons suggest that the oxide layer produces a modest deepening and enlargement of the transformed zone at comparable loads, consistent with a more confined subsurface stress field. The magnitude of this change remains within typical inter-laboratory variation, supporting the view that oxide confinement primarily modifies local transformation mechanics through boundary effects rather than altering the fundamental pressure thresholds or phase selection in silicon.

For spherical indentation at 200 mN, our oxide-capped samples exhibit a maximum indentation depth = 769 ± 3 nm and a residual depth $h_{residual}$ = 241.6 ± 3 nm. Reported bare-silicon data at comparable loads show similar depths, with our values exceeding typical lower-bound references by only a few percent in both h_{max} and $h_{residual}$.[21,22,28] These modest shifts, under a spherical contact, highlight the averaging effect of distributed contact stress: the influence of the oxide's local constraint is spread over a large contact area, so bulk geometric changes in depth are small. Nonetheless, consistently slightly larger residual depths and transformed volumes across different loads and indenter geometries are compatible with a coherent picture in which the oxide layer mildly deepens and enlarges the transformed zone by restricting lateral stress relaxation, while intrinsic pressure thresholds and phase-selection pathways in silicon remain effectively unchanged within experimental scatter.

At sufficiently high indentation loads, the nature of pressure-induced phase transformations in silicon changes fundamentally due to the substantial increase in the transformed volume beneath the indenter. Recent high-load spherical indentation studies have demonstrated that when the stressed volume extends to the μm-scale, the system is no longer limited to forming a small amorphous pocket; instead, extended crystalline domains can develop.[56,62,63] In particular, μm-sized hexagonal silicon crystals have been recovered following high-load spherical indentation combined with post-indentation annealing, highlighting the critical role of transformation volume in stabilizing ordered crystalline phases (R8 and BC8) during unloading.[62]

Consistent with this interpretation, the present study on silicon dioxide-capped silicon, using a 20 μm diameter tip for spherical indentation, reveals a complex dependence on the applied load. At a maximum load of 500 mN, a distinct pop-out event occurs at approximately 170 mN. In our earlier work on bare silicon at the same maximum load, the pop-out occurred at a higher unloading load of around 200 mN,[63] while Bikerouin *et al.*[62] and Johnson *et al.*[64] reported pop-out events at even higher loads, near 300 mN, for peak loads of 700 to 750 mN. Furthermore, when using a 13.5 micrometre tip, pop-out occurred at around 350 mN for 700 mN maximum load.[5] While these literature benchmark established that high-load spherical contact can create substantial transformed zones, approximately 10 μm in diameter, as shown by Johnson *et al.*,[64] the present TEM results indicate that the presence of the silicon dioxide cap significantly alters the internal stability of these zones.

Specifically, TEM observations show that a 200 mN load in the capped system facilitates the formation of a highly ordered crystalline transformation zone that is largely free of cracks and amorphous regions. In contrast, increasing the maximum load to 500 mN leads to a higher prevalence of amorphization and localized cracking. This behavior suggests that, although the silicon dioxide layer provides mechanical confinement consistent with the matrix constraints described by Ruffell *et al.*,[65] there exists an upper threshold beyond which the oxide-capped system can no longer accommodate the volumetric expansion associated with the β-Sn phase.

The systematic shift toward lower pop-out loads observed in the capped system confirms that the oxide layer stabilizes the denser β-Sn phase to lower unloading pressures. However, at the 500 mN load limit, the accumulated strain energy likely exceeds the stability window of the R8 and BC8 crystalline phases, favoring collapse into a disordered amorphous state and promoting fracture. This response contrasts with the predominantly single-mode deformation behavior reported by Wong *et al.*[59] for bare silicon and suggests that the silicon dioxide cap introduces a distinct interfacial stress state. This stress state appears to optimize crystalline recovery at moderate loads, around 200 mN, while promoting structural degradation at excessively high loads, around 500 mN. Together, these observations define a critical loading window for achieving controlled phase transformability under dielectric caps, in which the balance between mechanical confinement and total accumulated strain governs the final structural state of the recovered silicon.

Additionally, we calculated the intensity ratio of the R8 to BC8 phases from Raman spectroscopy measurements after indentation with varying loads. The results show that the R8/BC8 peak intensity ratio increases from approximately 1.5 at low loads to about 3.5 at the highest loads investigated. This trend suggests that the relative proportion of the R8 phase increases with higher indentation loads, potentially indicating a higher percentage of R8 present under these conditions.

However, it is important to note, consistent with previous reports in the literature, that the direct correspondence between Raman intensity and phase percentage is not straightforward. This is due to the unknown or varying Raman scattering cross-sections for the R8 and BC8 phases, as well as differences in their electronic structures. Studies such as Haberl *et al.*[57] have demonstrated that equal peak intensities may be observed even when the actual phase fractions are not equal, cautioning against a quantitative interpretation of the intensity ratio as a direct measure of phase content. Therefore, while the observed R8/BC8 intensity ratio can qualitatively reflect the evolution of phase composition with applied load, it may not be used to determine the absolute amounts of each phase without further calibration.

A similar trend in R8 and BC8 peak intensity ratios observed in this study has also been reported in the literature. Notably, the equivalence of these phase intensities is significant, as it indicates that the presence of oxide does not affect the intrinsic thermodynamic or kinetic preference for the formation of R8 or BC8 phases. If the oxide layer were to substantially modify the local pressure-stress environment, we would expect to see a noticeable shift in phase selectivity, such as an increase in R8 relative to BC8 under higher apparent pressures, or a preference for BC8 if the stress state became more hydrostatic. However, our results show no evidence of such shifts, supporting the interpretation that the oxide influences the system primarily through geometric confinement, which affects the distribution and depth of stresses, rather than altering the underlying phase stability of silicon.[33,66,67]

The most dramatic oxide effect appears not in phase transformation metrics but in fracture morphology. Oxide-capped Berkovich indents show "severe lateral + spallation" (100 mN) *versus* "median + lateral" cracking (bare Si),[26,27] while oxide-capped spherical indents exhibit "ring + cone cracks" *versus* "minimal/none" cracks (bare Si at 100 mN).[21,28] Quantitatively, this translates to earlier onset of oxide cracking (visible at 40–50 mN Berkovich *vs.* no cracking in bare Si at 50 mN (ref. 5 and 21)) and modified crack geometry (ring-cracks in oxide *vs.* radial-only in bare Si).

The mechanistic explanation is that the brittle oxide film (elastic modulus ~70 GPa, fracture toughness ~0.9 MPa $m^{0.5}$) is weaker than the underlying silicon substrate. Under the stress gradients imposed by indentation, the oxide cracks first, either through-thickness or along the Si/SiO_2 interface (delamination).[68] This does not prevent substrate phase transformation or fracture, our cross-sectional TEM (Fig. 4) shows that R8/BC8 phases formed directly beneath the fractured oxide, but it does deflect the damage pattern. The oxide acts as a "weak link" that fails first, displaying the visible crack signature while the silicon undergoes less obvious transformation and damage underneath. In practical terms, this means that post-indentation optical inspection of oxide crack patterns (radial *vs.* ring morphology) can serve as a proxy for the underlying substrate damage state, a useful diagnostic for devices.

Using the Oliver–Pharr contact mechanics method with measured depth values, we calculated mean contact pressures for all conditions (Table 1). For Berkovich, pressures range from 20.2–38.3 GPa depending on load; for spherical, from 11.8–23.1 GPa (reflecting the lower contact pressures of blunt geometry). Peak pressures beneath Berkovich apexes (applying 1.3–1.4 × stress concentration[24] yield estimates of 26–54 GPa), with the transformation threshold (~10–13 GPa hydrostatic equivalent) clearly exceeded even at low loads where pop-out events first appear. This is consistent with literature findings that the mean contact pressure at pop-out threshold for Berkovich on bare Si is 35–38 GPa (ref. 5 and 21) matching our oxide-capped value of 38.3 GPa at 50 mN. The critical hydrostatic pressure for dc-Si → β-Sn transformation is well-established at ~11–12 GPa from bulk experiments,[7,8] and our calculations confirm this is achieved at all tested loads with both indenters, supporting the occurrence of pop-in (loading) and pop-out (unloading) events as observed.

The lack of systematic pressure differences between oxide-capped and bare Si (differences <5% within calculation uncertainty) is the strongest evidence that the oxide modifies stress distribution (geometry, localization) but not the intrinsic pressure thresholds. If the oxide were mechanically coupled to the silicon in a way that altered peak pressure magnitudes (*e.g.*, by raising effective stiffness substantially), we would expect measurable shifts in the critical pop-out pressures or significant changes in the loads required to achieve measurable phase transformation. We observe neither.

Thus, Table 1 presents quantitative evidence that a thin (~285 nm) thermally grown oxide cap modifies the spatial and temporal aspects of silicon's indentation response, where transformation occurs (deeper), how large the transformed zone becomes (+10–15% volume), and how damage manifests at the surface (oxide cracks earlier, altering visible fracture patterns), without significantly altering the fundamental pressure thresholds or phase selectivity. Oxide effects are most pronounced under sharp (Berkovich) loading, where stress concentration amplifies any geometric constraint, and are muted under spherical geometry, where stress is distributed. These findings validate recent molecular dynamics predictions,[33] which suggest that oxide primarily acts as a boundary modifier, and they provide experimental validation for designing oxide-coated silicon systems in which phase transformation and mechanical reliability must both be considered.

4. Discussion

4.1. Deformation mechanisms and phase transformation pathways

Our experiments demonstrate that indenter geometry profoundly influences whether the SiO_2/Si system undergoes phase transformation or fracture at a given load. Sharp Berkovich indentation concentrates stress in a highly localized zone beneath the indenter tip, generating a steep hydrostatic pressure that rapidly exceeds the ~10–12 GPa threshold for the dc-Si → β-Sn phase transition. Even at modest loads (~40–50 mN), the Berkovich tip drives silicon into the high-

pressure β-Sn phase. Upon unloading, the trapped β-Sn releases stored energy *via* two competing pathways: (1) phase reversion to stable dc-Si through intermediate metastable structures, or (2) stress relief *via* cracking and localized plastic flow. Our results show that up to moderate loads (~50–60 mN), phase transformation dominates, evidenced by pronounced pop-out events and formation of crystalline R8/BC8 phases, with minimal observable surface fracture. This early phase transformation, preceding visible substrate cracking, indicates that shear strain plays a critical role in driving these structural transitions, a key insight supported by recent theoretical work showing that deviatoric stress can significantly lower energy barriers for phase transformation compared to purely hydrostatic conditions.[68,69] This supports the emerging view that pressure-induced phase transformations in covalently bonded materials like silicon can follow strain-dominated pathways under highly non-hydrostatic stress states, as further demonstrated in our recent work on crystalline-to-hexagonal silicon transitions under localized stress fields.[63] Thus, the sharp Berkovich indenter creates a strain-dominated, non-hydrostatic stress state that efficiently nucleates metastable polymorphs in silicon.

The formation of crystalline R8/BC8 at comparatively low mean pressures under Berkovich indentation reflects this strain-controlled pathway. Prior studies emphasized that sharp contacts generate high deviatoric stress components, favoring metastable polymorph nucleation at lower mean loads compared to blunt geometries.[6,70] Our Raman and TEM findings directly confirm this: strong R8/BC8 signals and minimal amorphous content appear at low loads under Berkovich, consistent with cross-sectional TEM studies showing completely crystalline transformation zones at ~50 mN peak load. This crystalline yield is enabled by the slow, controlled unloading protocol (typically 30 s from peak to zero load), which provides sufficient time for β-Sn → R8/BC8 solid-state crystallization rather than quenching into amorphous Si.[5,71] Thus, under sharp Berkovich indentation, silicon exhibits a brittle-to-quasi-ductile deformation transition: it first accommodates contact stress through phase transformation (analogous to localized ductile flow *via* volume collapse and re-expansion), but as the transformed zone expands with increasing load, cracking initiates at zone boundaries where tensile stresses concentrate. This competition between transformation-mediated energy absorption and brittle crack initiation explains the moderate loads (~100 mN) at which we observe significant oxide delamination and substrate fracture.

Beyond serving as a mechanically weak overlayer, thermally grown SiO_2 fundamentally alters the deformation pathway of silicon during indentation. Its relatively low stiffness (~70 GPa) and toughness (~0.9 MPa $m^{0.5}$) promote early cracking and interface delamination, but this failure is not merely detrimental; it modulates how stress is distributed and released beneath the surface.[68] The oxide initially constrains the silicon, extending the duration of subsurface stress accumulation and favoring the nucleation of metastable R8/BC8 phases. Once the interfacial adhesion limit is exceeded, however, the oxide redirects fracture along the Si/SiO_2 interface, effectively channelling energy away from the substrate. This interplay, between temporary confinement and selective damage release, explains the contrasting crack morphologies and transformation extents observed between Berkovich and spherical indentations (see section 4.2).

The sharp indenter's effectiveness at nucleating R8/BC8 at modest loads points toward a strain-controlled transformation mechanism rather than simple pressure dependence. Yesudhas *et al.*[66] demonstrated that localized shear deformation can lower energy barriers for phase transformation in silicon, favoring formation of metastable polymorphs like β-Sn and its crystalline descendants. In our system, the localized shear generated by the Berkovich indenter, possibly amplified by oxide constraint, likely facilitates the initial dc-Si → β-Sn transition during loading and subsequent R8/BC8 emergence upon unloading, providing the mechanistic basis for the pop-out events and Raman signatures we observe at modest loads. This interpretation is reinforced by the fact that spherical indentation, which generates a more hydrostatic stress field, delays observable transformation to substantially higher loads (~92 mN), a direct demonstration of how geometry controls the stress-state pathway and thus phase transformation selectivity. These findings reinforce that non-hydrostatic stress states, not peak pressure alone, determine the polymorphic evolution of silicon under contact loading.

4.2 Fracture behavior and film–substrate effects

Under spherical indentation, the deformation mechanism shifts toward more distributed elastic–plastic deformation with a delayed onset of fracture. The larger contact area of a spherical indenter produces a more uniform, predominantly hydrostatic stress field for a given load, compared to the highly concentrated stresses of a Berkovich tip. Silicon under a spherical indenter initially deforms elastically until a critical mean contact pressure is reached (on the order of 11–15 GPa for a ~20 μm radius tip), at which point an inelastic event occurs, typically manifesting as a sudden "pop-in" in the load–displacement curve associated with the dc-Si → β-Sn phase transformation, rather than immediate fracture. In our spherical indentation tests, we indeed observed an initial pop-in at ~40 mN (with no cracks visible at the surface), supporting the interpretation that the first yielding event in silicon is a phase change, not a crack. This agrees with Hertzian contact mechanics and finite element analyses, which indicate that for spherical contacts, the hydrostatic component of stress dominates in the indented volume, thereby delaying the development of the tensile stresses that nucleate cracks.[20] Once the high-pressure phase transformation begins under the spherical indenter, the silicon undergoes a substantial density change (the β-Sn phase is approximately 30–32% denser than dc-Si),[72,73] which contributes to a more plastic-like response. The spherical indenter also produced a distinctly larger transformed volume than the Berkovich indenter, a difference that reflects how the material accommodates deformation rather than where the peak pressure is located. Under spherical

loading, the silicon can deform more uniformly and densify over a wider lateral area before any fracture or stress release occurs, allowing a substantial portion of the plastic zone to enter metastable states. This is consistent with our Raman spectroscopy results at higher spherical loads (150–500 mN), where the R8/BC8 peaks were noticeably stronger than in Berkovich indents of comparable load, indicating a greater volume fraction of these phases.[74] Correspondingly, the residual spherical impressions exhibited broad, smoothly contoured deformation zones rather than the sharply tapered geometry characteristic of Berkovich indents, a morphology suggestive of a wide, bulb-like transformation region rather than the narrow, deeply penetrated zone typical of sharp contact.[21]

A crucial point for both indentation geometries is the interplay between phase transformation and fracture (brittle cracking). Silicon at room temperature has very limited ability to accommodate shear *via* conventional dislocation plasticity; thus, the pressure-induced phase transformation acts as the primary mode of inelastic deformation.[38] The volume collapse from dc-Si to β-Sn (and the subsequent re-expansion to R8/BC8 or amorphous Si upon unloading) absorbs a considerable amount of energy and relaxes stress, effectively delaying the onset of fracture.[6,75] Our results strongly reinforce this concept: in both Berkovich and spherical tests, we found that cracking was significantly delayed until after the phase transformations had occurred. In the Berkovich case, although some cracking began at relatively low loads (~40–50 mN) in the oxide layer (which we will discuss shortly), the silicon substrate beneath remained largely intact up to higher loads, often cracking only after a substantial transformed zone had already formed underneath. In the spherical case, we observed no surface cracking at all until about ~100 mN, by which point a sizeable volume of Si had transformed (as confirmed by post-indentation Raman analysis). This behavior is consistent with reports in the literature that a "ductile" phase transformation can precede and mitigate fracture in silicon. For instance, Bradby *et al.* have shown that it is possible to create fully phase-transformed zones under an indenter (consisting of crystalline high-pressure polymorphs) without any cracks, provided that the unloading is gentle and the transformation is allowed to proceed to completion.[28] In our spherical indents, up to a certain load, essentially all the deformation was accommodated *via* elastic–plastic flow and phase change, with cracking only initiating once the transformed zone and its associated volumetric changes grew large enough to induce tensile failure in the surrounding material.

When a fracture does eventually occur, its mode and progression differ markedly between the sharp and blunt indenter geometries,[76] and the presence of the surface oxide film further influences the cracking patterns. Berkovich indentations tend to produce the classic median-radial crack system known from indentation fracture mechanics of brittle materials. The extremely high contact pressure and steep stress gradients under a sharp indenter drive the formation of a so-called median crack, a subsurface crack roughly along the loading axis beneath the indent, almost as soon as the material yields in a brittle manner. Upon unloading, this median crack can extend to the surface, emerging as radial cracks emanating from the indent's edges or corners.[54,77] In our Berkovich tests, we indeed observed radial cracks originating from the three indent corners at relatively low loads, which is characteristic of this fracture mode. These appeared as soon as the critical load for crack nucleation was exceeded, owing to the large tensile hoop stresses at the indent perimeter for a sharp contact. According to classic indentation fracture theory (Lawn's model), the stress intensity at the indent corners rises quickly with applied load; once a threshold is reached, radial cracks nucleate and then lengthen with further loading and on unloading (driven by residual tensile stress).[76] The presence of radial cracks in all our Berkovich indents beyond ~40 mN is in line with prior reports that even within silicon's so-called "ductile" regime, some cracking is inevitable. For example, Zarudi *et al.* noted that median cracks were observed (*via* TEM) in all their indents (spherical or sharp) once a certain load was exceeded, even if those cracks did not always extend to the surface.[21] In our case, by ~100 mN the radial cracks in the silicon substrate had become long enough to cause serious substrate damage and to interact with the oxide film, eventually leading to film spallation around the indent.

Another hallmark of Berkovich-induced fracture is the formation of lateral cracks, which run roughly parallel to the surface (at some depth beneath the indent) and can cause the uplift or outright removal of material between the crack and the surface.[77] These lateral cracks are responsible for the plate-like fragments of oxide/silicon that were observed to be lifted or ejected around the larger Berkovich indents in our experiments. Once a lateral crack propagates outward beyond the indent impression, the material above it, in this case, the oxide film and a shallow layer of silicon, is effectively pried off. Our SEM examinations of Berkovich indent sites showed many such thin plates and flakes around the imprint, indicating multiple lateral cracks at different depths had occurred. The sudden propagation of a large lateral crack can also produce a discontinuity or sudden burst in the load–displacement curve, a phenomenon known as a "giant pop-in" if it occurs during loading. In our experiments, the pop-outs we observed at moderate loads were primarily due to phase transformations (β-Sn expanding to R8/BC8), but at the highest loads, we occasionally noted irregular, large pop-out events and load drops that we attribute to fracture events. For example, in one 150 mN Berkovich test, an abrupt ~300 nm increase in indent depth was recorded late in the unloading segment (beyond the usual smaller pop-out associated with phase change), likely corresponding to a fracture-induced stress release event similar in mechanism to the "giant pop-in" phenomenon described by Oliver *et al.*[78] (which they observed during loading), but occurring in the unload phase in our case. The important insight here is that fracture can compete with phase transformation as a mode of energy release: if a crack nucleates and propagates, it can rapidly relieve stress and consume energy that otherwise would have gone into driving phase transformations.[49] This competitive interplay might explain some of the variability in

our load–displacement curves (*e.g.*, why some indents showed multiple or suppressed pop-outs). In the Berkovich case, the stress state strongly favors crack formation (high shear stresses and tension at the edges of the plastic zone),[21] so we see earlier crack initiation and more energy diverted into crack growth, which in turn can limit the volume of transformed Si. In extreme cases, a large crack event can abruptly terminate the retention of high-pressure phase by quickly unloading the stress.

Spherical indentation, on the other hand, delays the onset of cracking and favors a different crack geometry once fracture finally begins. Owing to the more equibiaxial nature of the contact, a ring crack (Hertzian cone crack) is the preferred fracture mode in brittle materials under spherical loading.[34,79] For an ideal brittle half-space indented by a sphere, a ring crack tends to initiate at the edge of the contact circle (where the tensile stress is highest upon unloading) and then propagate downward at an angle, forming a cone-shaped crack front.[80] In our coated system, we observed precisely this behavior in the oxide film: circular ring cracks formed around the perimeter of the contact area in the SiO_2 layer. These ring cracks in the film are analogous to Hertzian ring cracks in glasses or ceramics, but they occurred in a layered context, often initiating in the film and sometimes arresting at the film/substrate interface or deflecting along that interface. The ring cracks became more pronounced and numerous with increasing load, as expected, since the contact radius (and thus the circumference of the high-stress region) grows with load, increasing the probability of a flaw or weak point triggering a crack. Once a ring crack formed in our samples, it often extended downward into the substrate as a shallow cone crack or spread laterally along the Si/SiO_2 interface.[81,82] Our SEM evidence at 500 mN, for instance, shows that some ring cracks in the oxide had turned into partial cone cracks in the silicon (producing a shell-like spallation of the substrate beneath the film). However, because the silicon had undergone considerable inelastic deformation *via* phase transformation by that point, these cone cracks were less deep and contained compared to what one would expect in a purely elastic, brittle indentation. Notably, even at 500 mN the spherical indent did not produce the kind of catastrophic, far-reaching crack network that the 100 mN Berkovich indent did. Instead, the damage from the sphere was largely confined to a delaminated "doughnut-shaped" region around the indent, where the oxide detached but the substrate cracking was relatively contained. This illustrates the spherical indenter's ability to distribute damage over a larger area, thereby avoiding the deep, concentrated cracking seen with sharp indenters. It also underscores that fracture under spherical indentation is a delayed and somewhat stochastic event. Oliver *et al.* reported a wide scatter in the load at which silicon exhibits a large crack-induced pop-in under spherical indentation (with a ~4–5 μm tip radius, they found a threshold around 350 ± 100 mN for a major crack event, and "giant" pop-ins typically at loads beyond 500 mN).[83] In our tests, we similarly observed that some spherical indents could be pushed to very high loads with only minor cracking, while others at comparable loads experienced a sudden crack-induced spallation of the oxide and underlying silicon. This variability is characteristic of crack nucleation, which is highly sensitive to the presence of flaws and slight differences in local stress distribution.

The 285 nm thermal SiO_2 film on the silicon adds an important layer of complexity to the fracture behavior. Although thin, this oxide is much less compliant than the silicon substrate and has its own fracture properties. Prior atomistic simulations have shown that amorphous SiO_2 under nanoindentation does not behave as a perfectly elastic, brittle layer; instead, it can undergo local densification, shear flow, and network collapse under high contact pressures. For example, Chen *et al.* used molecular dynamics to demonstrate that when thin silica layers are indented, the Si–O network can compact along the loading axis, leading to permanent densification of the film.[33] This not only thins the film locally but also alters the stress distribution transmitted to the underlying silicon. Their simulations indicated that at lower indentation rates, such densification can delay crack initiation, whereas at higher rates or higher loads, through-thickness cracks in the film become more likely as the material has less time to flow.[84] In our experiments, we did not directly measure densification in the oxide, but several observations are consistent with this phenomenon: the appearance of interference fringes (Newton rings) around some indents, circular film delamination patterns, and blister-like uplift of the film all suggest that the oxide underwent out-of-plane deformation (thickness change) and partial debonding. We did not see significant pile-up or plastic flow of the oxide around the indent perimeters, which implies that the SiO_2 primarily accommodated the stress by densifying in the thickness direction and by cracking/delaminating, rather than by lateral plastic flow. Therefore, the oxide layer plays a dual mechanical role: it transiently constrains the silicon surface (affecting the pressure needed for phase transformation), and it also acts as a brittle veneer that can crack or delaminate under the induced stresses.

One immediate effect of the film is to act as a brittle layer that cracks readily once the underlying silicon undergoes sufficient deformation.[34,85] We observed that many of the first visible cracks during indentation were in the oxide itself (for example, the radial cracks emanating from Berkovich indent corners often corresponded to splits in the oxide film). These film cracks can then either continue propagating into the substrate or deflect along the interface, extremely shallow median cracks in the silicon by adding surface compressive stress (*i.e.*, the film can hold the very top surface in compression to some degree), but at only 285 nm thickness its influence on the subsurface stress field is minor. However, it does significantly influence how and where damage manifests at the surface. Instead of an open, penny-shaped crack directly in the silicon, we often observed delamination: the film would debond from the substrate when a lateral crack formed or when tensile stresses at the interface exceeded the adhesion strength. Our observations of multi-coloured interference patterns and blister-like buckling of the film are clear signs that the oxide detached locally from the silicon. In some cases, we saw the oxide film

remain largely intact but bow upward (like a blister), indicating that a crack had propagated along the Si/SiO_2 interface (an interfacial delamination) without the film itself fully fracturing. In other cases, the film was fractured into segments, suggesting that through-thickness film cracks occurred in combination with interface cracks, thereby isolating small chunks of the film. Whether the oxide tends to fracture through its thickness or to delaminate (or both) depends on the stress state. Under the sharp Berkovich indenter, the film experienced highly localized bending and stretching, causing it to crack at relatively low loads (hence the early radial cracks in the film). Under the spherical indenter, the film was subjected to a broader, more uniform flexure upon unloading, leading predominantly to circular delamination (ring cracks) at higher loads. In both cases, once the film cracked or debonded, it absorbed some energy but did not prevent the substrate from eventually cracking; rather, it altered the mode of failure. When the substrate did fracture, the film often came off with it or after it.[85] Thus, the oxide did not arrest substrate cracks; it either cracked first or let go from the substrate, so that the silicon crack could propagate unimpeded along or beneath the interface.

From a fracture mechanics perspective, the presence of the thin film creates an additional interface fracture problem on top of the normal indentation fracture modes. We essentially have a trilayer system (oxide film, film/substrate interface, and silicon substrate) where mismatches in deformation can generate interface cracks (delamination) or cause cracks to jump from one layer to another. Indeed, many of the lateral cracks we infer in our indents likely propagated along or near the Si/SiO_2 interface.[32,34,78,86] The small "chips" we observed, pieces of oxide attached to a thin layer of silicon that spalled off together, imply that some cracks initiated within the silicon and then deflected into the interface, prying off a combined chunk of film and substrate. Such complex crack paths are typical in brittle film/substrate systems under contact loading; thin films often fail by spalling in tile-like patterns, rather than a single neat cone crack, especially if the film is not strongly adhered. The practical consequence in our system is that the oxide does not appreciably protect the silicon from mechanical damage under point loading; rather, it modifies the damage morphology. In our tests, the oxide layer did not prevent the high-pressure phase transformations in Si from occurring (since the silicon still reached the required pressure beneath the film), nor did it prevent substrate fracture (since cracks either went through the film or circumvented it *via* the interface).[32,85] What the oxide did do was cause a lot of the damage to appear as shallow, surface-level film cracking and delamination, instead of directly as deep substrate cracks. In an applied context (*e.g.*, a silicon device with a surface oxide or glass passivation layer), this means that at lower loads the initial mechanical failure might be primarily in the film (which could be benign for device operation if it's just cosmetic cracking), but if the load increases further the substrate can still fail just the same. It also means that inspecting the film's crack pattern (for instance, the presence of radial cracks or ring cracks in the oxide) can provide insight into the underlying substrate damage state before that substrate damage becomes visible.

4.3 Comparison with prior work

Our findings align well with the established literature on indentation-induced phase transformations and cracking in silicon, while also adding new nuance for the case of thin-film-coated surfaces. For example, Bradby and co-workers extensively studied phase transformations in indented silicon using Raman spectroscopy and showed that the appearance of metastable R8/BC8 phases correlates directly with pop-in and pop-out events in the load–displacement curve.[70] We observed the same correlation in our experiments: a pop-out event upon unloading is a signature of β-Sn reverting to lower-pressure phases (R8 and/or BC8), which we then confirmed by the presence of their characteristic Raman peaks (~166 cm^{-1}, ~353 cm^{-1}, ~398 cm^{-1} for R8, and ~378 cm^{-1}, ~442 cm^{-1} for BC8).[39,44] In agreement with Juliano *et al.* and other studies, we found that using a slower unloading rate favors the formation of these crystalline polymorphs (R8/BC8) rather than trapping the material in a completely amorphous state.[40,71] Indeed, our standard unload schedule (which was not excessively fast) allowed for ample R8/BC8 formation in both Berkovich and spherical indents, rather than producing only amorphous Si, this is why we often obtained a mixed phase zone under the indents. The presence of such mixed-phase zones (containing both amorphous and crystalline high-pressure phases) is consistent with the mixed-mode deformation observed by Domnich & Gogotsi in their indentation experiments and molecular dynamics simulations of silicon under load.[6,15] Those authors noted that silicon's response to contact loading can be viewed as a competition between reversible phase changes (to metastable crystalline phases) and irreversible amorphization, with the outcome depending on the precise stress state and loading conditions. In our case, the sharp Berkovich indenter favored the reversible (crystalline) transformation pathway at comparatively lower loads than the spherical indenter did, but ultimately both indenter types produced similar phase assemblages in the silicon; only the size and geometry of the transformed zones differed.

The spatial distribution of phases within the indent-affected zone also shows excellent agreement with prior observations. Zarudi *et al.*[21] performed cross-sectional TEM on indented silicon and reported that for a Berkovich indent, the crystalline high-pressure phases (BC8 and R8 silicon) tend to reside at the bottom of the transfo6rmed zone (with a thin amorphous region nearer the surface), whereas for a spherical indent the crystalline phases were found closer to the top surface, roughly in the middle of the plastic zone. They attributed this to the different stress fields: a sharp indenter produces a highly concentrated hydrostatic pressure region deep beneath the tip and high shear stresses near the surface, whereas a spherical indenter's stress field is more hydrostatic-dominated at a shallower depth and spreads over a larger area.[20,81,87] Our post-indentation analyses are in line with this

framework. For example, a Berkovich indent that showed strong Raman signals of R8/BC8 also exhibited a minor amorphous Si signal, implying that a thin amorphous layer likely formed closer to the surface above the crystalline transformed region. This suggests a depth-dependent transformation behavior, where the deeper region crystallizes into metastable phases while the near-surface layer may amorphize due to faster stress relaxation and limited volume confinement. In contrast, a spherical indent at the same load produced a broader Raman signal distribution and a relatively larger amorphous component, suggesting the transformed zone was more laterally distributed and possibly included amorphous regions mixed with crystalline phases throughout.[42] These subtle differences in phase distribution are important because they influence where cracks are likely to nucleate, cracks often originate at the edges of the transformed zone due to volume changes or stress concentrations at phase boundaries.[49] Thus, the indenter geometry not only affects whether silicon undergoes phase change or cracking, but also where within the material these processes occur, which in turn governs the subsequent fracture path.

The observed crack patterns in our experiments also illustrate classical principles of indentation fracture mechanics. As discussed by Lawn and co-workers in the 1970s–80s,[88] a sharp indenter on a brittle material will produce radial-median cracks at relatively low loads, and with increasing load, lateral cracks can form and cause material removal (sometimes termed "chipping" or spalling).[83,89] We saw exactly this progression with the Berkovich indenter: radial cracks appeared starting around the threshold load (~40–50 mN for silicon with our tip), and at higher loads these evolved into extensive lateral cracking that caused portions of the film and substrate to break free (by ~100–150 mN, significant pieces of the oxide and even substrate had spalled out around the indent). In contrast, a blunter contact (like our spherical tip) tends to suppress cracking to higher loads and then typically produces a Hertzian cone crack pattern instead of radial cracks. Our observation of ring cracks in the oxide and eventual shallow cone cracking in the substrate at high spherical loads is in line with this behavior. In fact, the absence of any radial cracks emanating from the spherical indents until very high loads, and even then only in combination with a ring/cone crack, is consistent with the expectation that a spherical indenter (especially on a somewhat ductile-response material like phase-transforming silicon) will not generate radial cracks unless a large, unstable fracture event occurs.[78,90] Lawn's analyses predict that the critical load for radial (median) cracking increases dramatically with indenter bluntness; in an ideal scenario, a sufficiently large spherical indenter produces only a ring/cone crack upon unloading rather than radial cracks during loading.[88] This helps explain why we didn't see classical radial cracks in the spherical case until the loads were quite high, and even then, the cracks were part of a broader cone crack that caused delamination rather than sharp radial fissures from the contact edge. Furthermore, our high-load spherical tests occasionally showed crack-induced displacement bursts during loading, consistent with observations by Oliver *et al.*[83] for instance, one ~450 mN spherical test exhibited an abrupt depth excursion of ~500 nm during loading, accompanied by shattering of the oxide film, a clear sign of a sudden crack event (likely a lateral crack or rapid cone crack propagation) leading to a loss of support under the indenter. Oliver *et al.*[83] attributed such phenomena in Si and Ge to the rapid propagation of lateral cracks that remove material under the indenter, and our observations support that mechanism as well. Even with a spherical indenter, once a crack is initiated, it can lead to a violent failure mode and a large displacement burst.

4.4 Cross-sectional microscopic evidence and further analysis

The cross-sectional micrographs in Fig. 3 illustrate how indenter geometry influences crack formation and deformation beneath the oxide film, directly supporting the discussion above. At a lower representative load (*e.g.*, 200 mN), the spherical indent produces a confined deformation zone in the silicon with minimal cracking, whereas even at a much lower load (100 mN) the Berkovich indent shows clear median and radial cracks propagating from the indent site into the substrate. This confirms experimentally that the sharper Berkovich tip induces cracking at significantly lower loads than a blunt tip, consistent with our earlier reasoning and with literature expectations (indeed, a through-thickness crack observed at 100 mN would be unexpected if the indenter were spherical, highlighting the brittleness triggered by the sharp tip). At higher loads (*e.g.*, 500 mN), both indenters cause more extensive damage, but of different character: the spherical indent generates some lateral cracking, notably along the SiO_2/Si interface (leading to a circular delamination of the film), while the sharp Berkovich indent induces severe cracking including full film spallation and deep radial cracks in the substrate. The greater stress concentration from the Berkovich tip likely accounts for the oxide film's complete detachment in that case, as a sharp indenter produces higher local tensile stresses and abrupt stress gradients that promote fracture and interface failure. Overall, the cross-sections in Fig. 3 reinforce our earlier claims of a more "ductile", crack-suppressing deformation under spherical indentation *versus* a more "brittle" response under sharp indentation. The oxide layer in the spherical case remains largely intact at intermediate loads and helps confine the transformed zone (delaying crack onset), whereas in the Berkovich case, the oxide is breached early, and cracks run into and along the interface readily. This behavior aligns with the known reduction in crack initiation threshold for sharp pyramidal indenters compared to spherical ones,[21] and it highlights the role of the surface film in deflecting and channeling cracks (for instance, many of the lateral cracks in the silicon traveled along the weak Si/SiO_2 interface, eventually causing the film to blister or spall at higher loads).

Fig. 4 provides compelling TEM evidence of the pressure-induced phase transformations in the indent zones, further validating our interpretations. Selected-area electron diffrac-

tion patterns from beneath both spherical and Berkovich indents (Fig. 4e–h) confirm the formation of metastable crystalline Si phases. The measured interplanar spacings (~3.2 Å, 2.6 Å corresponding to R8 reflections and 2.3 Å corresponding to BC8 reflections in various diffraction rings) indicate that the indented material has transformed from the original dc-Si into a mixture of these high-pressure polymorphs. This direct structural identification solidifies our earlier inference (based on pop-out events and Raman spectra) that a high-pressure phase transformation occurred during indentation. Notably, the diffraction patterns show fairly sharp rings and little to no amorphous halo, indicating that the transformed zones are largely crystalline rather than amorphous. Such an outcome is expected under appropriate loading/unloading conditions: previous studies have shown that slower unload rates or higher peak loads favor the formation of crystalline metastable phases over amorphization.[21,70] The TEM results confirm that, for both indenter types, the material beneath the indent was driven into the β-Sn phase during loading and then relaxed into mostly R8/BC8 upon unloading (as opposed to ending up as amorphous Si). Furthermore, we observe that the size of the R8/BC8 crystallites in the high-load indents is on the order of hundreds of nanometres, consistent with the trend that higher indentation loads (and larger transformed volumes) produce larger crystalline domains in the transformed zone.

Importantly, Fig. 3 and 4 together illustrate how indenter geometry affects not just whether phase transformations occur, but where they occur and how they interact with the oxide film. The bright-field TEM cross-sections (Fig. 4a–d) reveal that in the spherical indentation cases, the R8/BC8 phase region lies relatively close to the surface (just beneath the intact SiO_2 layer), whereas for the Berkovich cases the R8/BC8 region is situated deeper in the silicon, often with a thinner (or partially amorphized) zone near the top surface. This distinction matches the mechanism proposed in the literature: under a sharp indenter, the highest hydrostatic pressure (which drives R8/BC8 formation) occurs below the indenter tip, beneath a region of intense shear and likely amorphization near the surface, so the crystalline phase ends up at the bottom of the transformed zone.[61] In contrast, a spherical indenter generates a more uniform, hydrostatic-dominated stress field that allows the crystalline high-pressure phases to form closer to the surface, roughly in the mid-depth of the plastic zone.[21] Our observations agree with this framework: for example, the spherical 200 mN indent shows an R8/BC8 zone directly under the oxide, whereas the 100 mN Berkovich indent shows the crystalline phase only in the deeper portion of the affected region (with evidence of a shallow amorphous layer above it). The presence of an intact oxide in the spherical case likely further enhanced the hydrostatic confinement, promoting a broad, shallow transformation zone. By constraining the silicon, the oxide layer helped suppress early surface cracking and facilitated the growth of R8/BC8 crystals near the surface. In the Berkovich case, however, the oxide was cracked and partially delaminated early on, so the top of the indent zone experienced some stress relaxation (and the formation of amorphous Si), thereby relegating the crystalline phase formation to greater depths, a scenario consistent with prior comparative studies of Berkovich *vs.* spherical indentation in silicon.[21]

The high-resolution TEM images (Fig. 4i–l) shed additional light on the interface and defect structures resulting from these different deformation modes. In the spherical indent scenario at moderate load, we observe a relatively well-preserved trilayer structure: the SiO_2 film remains adherent on top of a transformed R8/BC8 silicon layer, which in turn interfaces coherently with the underlying pristine Si substrate. The HRTEM image of this interface (*e.g.*, Fig. 4i) suggests a semi-coherent boundary between the R8/BC8 region and the original diamond-cubic lattice, with no large voids or gaps, implying that the phase transformation occurred *in situ* without completely losing lattice registry with the substrate. This could explain why, despite the large volume change associated with forming the denser β-Sn (and then the less dense R8/BC8), the oxide did not spall at 200 mN, the compressive confinement and surrounding elastic matrix accommodated the expansion to some extent, and the interface remained intact. By contrast, in the 500 mN Berkovich indent, the images show that the SiO_2 layer has delaminated and the transformed zone is exposed. The corresponding HRTEM view (Fig. 4j) reveals a high density of defects (dislocations, small cracks, or voids) at the interface between the transformed region and the remaining substrate. This extensive damage at the interface is a direct consequence of the violent stress release in the sharp indent case: once a lateral crack propagated and the oxide debonded, the R8/BC8 region was suddenly free to expand without constraint, but that rapid expansion (and the lack of an intact capping layer) introduced significant misfit strain, generating dislocations and microcracks at the boundary with the surrounding pristine silicon. Such defects are absent or far less pronounced in the well-confined spherical indent case (Fig. 4k–l), highlighting that a more homogeneous, hydrostatic-driven transformation (as achieved under the spherical tip with the oxide intact) leads to fewer interfacial flaws. These findings reinforce two key points of our study: (i) that phase transformation-induced "ductile" deformation can effectively suppress cracking when the stress state is close to hydrostatic (as we achieved with a spherical indenter and an intact surface film), and (ii) that when cracking does occur, it profoundly alters the outcome, causing film delamination and concentrated damage at interfaces, although the silicon still undergoes phase transformations in regions where the pressure was sufficient. Hence, the cross-sectional evidence from Fig. 3 and 4 strongly supports our earlier arguments by directly linking the mechanical events we recorded (pop-ins, pop-outs, crack patterns) to the underlying material changes (formation and distribution of metastable Si phases and crack propagation paths), in full agreement with the established understanding of silicon's behavior under contact stress.[21,91] The observed delamination and lateral cracking behavior align with mixed-mode failure mechanisms in thin films described by Hutchinson and Suo, where interfacial shear and tensile stres-

ses drive crack propagation parallel to and along the interface.[92]

4.5 Functional role of oxide constraint

The 285 nm thermal SiO_2 cap plays a complex dual role in modulating phase transformation and fracture behavior in the underlying silicon substrate. While our study shows that the oxide does not fundamentally alter the critical pressures for phase transitions,[5,21] its presence introduces both mechanical advantages and disadvantages that merit explicit discussion. Understanding this trade-off is essential for designing oxide-capped Si systems that maximize subsurface R8/BC8 formation while minimizing fracture damage, a key consideration for stress-engineered silicon applications in photonics, sensing, and advanced microelectronics.

The most significant advantage of the oxide cap is that it provides elastic constraint that promotes crystalline R8/BC8 formation over amorphization. This effect manifests mechanically in two distinct ways. First, the oxide acts as a stiff capping layer that supports the silicon surface, reducing the relaxation rate during unloading and thereby favoring slow, controlled phase decomposition of the high-pressure β-Sn phase into crystalline rather than glassy products. Literature studies have established that amorphization is favored by rapid stress relief, whereas slower unloading, characterized by extended time for atomic rearrangement within mechanical constraints, promotes crystalline polymorph formation.[59,93] This shift toward higher crystallinity is not attributable to changes in indentation load or pressure, since the pop-out thresholds (42 mN for Berkovich, 92 mN for spherical) match published values for uncoated silicon[5,21,74] but rather to the oxide's elastic constraint modulating the unloading kinetics. The mechanical origin of this effect lies in the oxide's modulus mismatch: the SiO_2 film ($E \sim 70$ GPa) acts as a constraint that reduces the outward stress-relief velocity compared to bare Si (where surface stress can relax freely). This slower relaxation rate allows the metastable β-Sn phase more time to undergo solid-state crystallization into R8/BC8 within the confined pressure field before it is quenched, whereas rapid unloading would trap the structure in an amorphous state.[72,73]

A second major advantage is that the oxide's delayed failure enables larger subsurface transformation volumes to develop while confinement remains intact. Under spherical indentation in particular, the oxide remains largely intact up to moderate loads (~200 mN, as seen in optical and SEM images, Fig. 3a), providing sustained elastic constraint to the transforming silicon throughout extended portions of the loading–unloading cycle. Our cross-sectional transmission electron microscopy analysis (Fig. 4c and d) reveals that under a 200 mN spherical indent, the estimated transformed zone volume is approximately 8–9 μm^3, based on the measured transformed depth of 528 nm (Table 1) and calculated contact radius of ~70 nm using Hertzian contact geometry.[70,94] This volume is comparable to literature estimates for bare Si at equivalent loads (~8–9 μm^3 from Zarudi *et al.*),[21] suggesting that the oxide enables sustained development of transformation zones to sizes equivalent to or slightly larger than accessible under uncoated conditions. Importantly, this sustained confinement during spherical loading produces more spatially uniform crystallinity throughout the transformed region, whereas sharp Berkovich indentation breaches the oxide earlier (~40–50 mN, coinciding with the pop-out event), truncating the confinement phase. The result is a clear geometric segregation of phases within the Berkovich indent zone (amorphous and mixed phases near the surface, crystalline R8/BC8 concentrated at depth) that is largely absent in the spherical case, where more uniform high-crystallinity phases throughout the transformed region reflect sustained confining support. This phase-distribution difference has practical significance for applications seeking to engineer large, stable high-pressure phase domains: spherical loading geometries with intact oxide caps can produce crystalline R8/BC8 zones on the order of 8–10 μm^3, substantially larger than the more heterogeneous zones accessible under sharp contact.

A third advantage of the oxide layer is its protective function against surface contamination and oxidative degradation. The intact thermal SiO_2 film shields the metastable R8/BC8 phases from atmospheric moisture, oxygen, and impurities during the indentation experiment and subsequent handling or device integration. This is particularly important since R8/BC8 Si are thermodynamically unstable at ambient conditions and can back-transform or undergo surface oxidation if exposed to air. From a contact-mechanics perspective, the oxide also provides a compliant intermediate layer that softens the initial tip-surface interaction: a sharp indenter initially penetrates the oxide before reaching crystalline Si, thereby reducing the extreme stress concentrations that would otherwise develop under direct tip-Si contact. This compliance buffer marginally reduces peak hydrostatic pressures at early contact stages, contributing to the observed reduction in amorphization during early-stage loading phases.

While the oxide confers substantial mechanical benefits, it simultaneously introduces significant disadvantages that complicate the stress field and introduce competing failure modes. The most fundamental disadvantage stems from elastic mismatch and film/substrate heterogeneity. The oxide's Young's modulus (~70 GPa) differs substantially from silicon (~170 GPa), causing stress field redistribution and creating regions of high stress concentration at the Si/SiO_2 interface. Our cross-sectional TEM analysis (Fig. 4b, d, f and h) shows that at high loads, this mismatch generates pronounced lattice distortion, dislocation tangles, and localized void accumulation along the film/substrate boundary, particularly in the Berkovich case, where the asymmetric, highly concentrated stress field amplifies interface stresses. Such defects serve as preferential crack-nucleation sites, accelerating premature failure of the interface even as the underlying Si undergoes phase transformation. This stress concentration is particularly severe under sharp Berkovich geometry, where the steep pressure gradients and deviatoric stresses create shear-dominated conditions at the interface.

A second major disadvantage is that the oxide introduces interfacial delamination as a competing and often dominant

failure mode. Because thermal SiO_2/Si interfaces have relatively weak adhesion energies (0.4–2.4 J m^{-2}, depending on interface preparation and oxide stoichiometry), and because the oxide is inherently brittle (fracture toughness <1 MPa $m^{0.5}$), the film readily delaminates under shear or tension stresses.[95] Our experimental observations consistently show that lateral cracks routinely propagate along the Si/SiO_2 interface, causing the oxide to spall in characteristic tile-like or annular fragments (particularly evident in SEM images of indents at high loads, Fig. 3c and d). This delamination becomes a primary failure mode, especially under the asymmetric stress field of a sharp indenter, where shear stresses along the interface are maximized. Once the film detaches and lifts away from the substrate, the silicon's high-pressure phase region is suddenly exposed to atmospheric pressure and oxygen, potentially triggering rapid back-transformation of metastable R8/BC8 phases to thermodynamically stable diamond-cubic dc-Si or surface oxidation, thereby destroying the engineered phase architecture. Furthermore, the energy dissipated in oxide cracking, delamination, and spallation represents a significant sink that reduces the elastic energy available for controlled phase transformation, possibly explaining the smaller R8/BC8-transformed volumes we observe at very high Berkovich loads (300–500 mN) compared to equivalent spherical loads, the difference reflects that sharp-indenter fracture occurs earlier and more catastrophically, consuming mechanical energy rather than preserving it within the high-pressure phase region.

A third major limitation arises from premature oxide cracking, which releases the applied constraint too early and restricts the growth of deep, extended transformation zones. Although the oxide initially provides strong confinement, its early failure reverses this effect by causing an abrupt stress drop. In our Berkovich experiments, oxide fracture occurs at relatively low loads (~40–50 mN), coinciding with or immediately following the pop-out event. This early loss of confinement allows the upper portion of the β-Sn region, closest to the oxide/Si interface, to relax before it can reorganize into coherent R8/BC8 domains. Consequently, Berkovich indents exhibit a distinctly stratified phase distribution: amorphous material dominates near the surface where stress was released first, while crystalline R8/BC8 forms only at greater depths where confinement persisted longer.

In contrast, spherical indentation delays oxide cracking to much higher loads (~200–250 mN; Fig. 3a), enabling the silicon to sustain confinement over a larger volume and for a longer duration. This results in more uniform transformed zones, higher overall R8/BC8 yield, and reduced amorphous content. These trends are fully consistent with our Raman and TEM data (Table 1 and Fig. 2, 4), which show surface-localized amorphization in Berkovich indents and relatively homogeneous crystalline transformation under spherical loading. In terms of the underlying mechanism early oxide fracture in the Berkovich case creates an efficient stress-release pathway, through delamination and through-thickness cracking, that dissipates the steep pressure gradient faster than the kinetics of solid-state crystallization (~10–100 ms). This rapid relaxation quenches the β-Sn phase into an amorphous product. Under spherical loading, the broader pressure field and delayed oxide failure allow crystallization to proceed before stress is released, favoring the formation of metastable R8/BC8 polymorphs throughout the transformed zone.

The advantages and disadvantages of the oxide layer present a clear trade-off scenario that fundamentally shapes optimal device design for stress-engineered silicon. At moderate loads (~50–200 mN) under spherical indentation, the intact oxide provides highly beneficial confinement, promoting formation of large, uniform, crystalline R8/BC8 zones with minimal amorphization. At low loads (~30–50 mN) under sharp indentation, early oxide cracking severely limits the utility of confining pressure; amorphization becomes significant, and transformed volumes remain smaller. At very high loads (>300 mN), both geometries eventually induce catastrophic oxide failure and severe interfacial cracking, overwhelming any confining benefit and triggering substrate spallation.[34,85] This trade-off has direct implications for stress-engineered silicon applications: if the goal is to stabilize large, subsurface R8/BC8 phases without fracture damage, system design should prioritize blunt loading geometries (spherical indenters or distributed contacts) combined with sufficiently large contact radii (>10 μm) to keep contact pressures moderate. Conversely, if sharp or highly localized contacts are unavoidable (*e.g.*, in wafer probing, scribing, or engineered stress applications), thicker or tougher oxide coatings, or oxide interlayers with enhanced adhesion, may be necessary to extend the confinement phase and thereby enhance R8/BC8 yield while suppressing premature substrate failure. Future systematic studies exploring oxide thickness variations and interface engineering strategies could optimize this balance for next-generation stress-engineered silicon devices.

4.6 Oxide thickness, unloading rate, and stress confinement framework

Our unloading segment was fixed at 30 s from peak load to zero. For Berkovich indentation, the pop-out (phase-transformation) event occurred at a maximum load of ~42 mN, giving an average unloading rate of ~1.4 mN s^{-1}. For the highest-load experiments using both spherical and Berkovich tips, where the maximum applied load was 500 mN, the corresponding unloading rate was ~16.7 mN s^{-1}. These rates fall squarely within the "slow unloading" regime defined by literature studies of silicon indentation kinetics. Fujisawa *et al.* established experimentally that R8/BC8 crystalline phases are favored at unloading rates below 50 mN s^{-1}, whereas amorphization dominates when unloading exceeds 100 mN s^{-1}.[71,96] Our measured rates (1.4–16.7 mN s^{-1}) are well below the 50 mN s^{-1} amorphization threshold, confirming that slow unloading kinetics are maintained throughout our experiments. This mechanical condition is essential because it allows solid-state phase crystallization, a diffusion-mediated process occurring over timescales of approximately 10–100 ms, to compete effectively with stress relaxation. Under rapid

unloading (>100 mN s^{-1}), the high-pressure β-Sn phase is quenched too quickly for crystallization to occur, trapping the structure in an amorphous state. Our slower rates provide the necessary temporal window for atomic rearrangement within the constrained pressure field, enabling R8/BC8 formation.

The oxide layer amplifies this crystallization advantage by further slowing stress-relief kinetics during unloading. As detailed in section 4.5, our oxide-coated system exhibits higher R8/BC8 content (I_{353}/I_{441} values in Table 1) ranging from 1.07–3.36 depending on load, compared to literature bare Si values of 1.0–3.5 at matched conditions[22,97] and correspondingly lower amorphous content. This enhancement arises because the SiO_2 cap (Young's modulus $E \sim 70$ GPa) acts as an elastic boundary that reduces the outward normal-stress-relief velocity compared to bare Si, where surface stress relaxes freely into air. Because the oxide remains largely intact during the 30 s unloading phase (oxide cracking occurs following the pop-out event, during hold and early unload stages), the Si substrate remains elastically constrained throughout much of the phase-crystallization window. This extended constraint period effectively elongates the accessible crystallization timescale, allowing more atoms to complete the β-Sn → R8/BC8 transition before the pressure field collapses. The synergistic effect of slow mechanical unloading rate, our 30 s protocol[5,70] combined with oxide elastic constraint, therefore powerfully promotes R8/BC8 crystallization, explaining the quantitative enhancement in Raman signatures observed in Table 1.

While we did not systematically vary oxide thickness experimentally due to time constraints, the literature on oxide-constrained silicon indentation provides instructive insights into thickness effects. Atomistic MD simulations (*e.g.*, Chen *et al.*, 2018)[31] clearly show that ultra-thin SiO_2 layers (0.4–2.0 nm) tend to fail early during indentation and therefore offer limited confinement of the underlying silicon. Experimental and continuum-scale studies on thicker SiO_2 films (spanning tens to hundreds of nanometres) report the same overall thickness dependence, although the exact transition point varies with oxide microstructure, adhesion, and indenter geometry. Moderate oxides (50–200 nm) provide intermediate confinement, delaying oxide fracture until higher loads and enabling broader transformation zones with mixed R8/BC8 and amorphous content. Thick oxides (>200 nm) provide sustained constraint, maintaining pressure support to substantially higher loads (200–400 mN depending on geometry) and strongly favoring R8/BC8 over amorphization. Our experimental 285 nm oxide thickness falls in the "thick" regime, consistent with our observation of sustained R8/BC8 formation to 200 mN under spherical indentation and high crystallinity throughout the transformed zones.

The oxide-thickness findings have practical design implications for stress-engineered silicon. Atomistic MD and nanoindentation studies reproduce the trend that very thin SiO_2 caps fail early and provide limited confinement (MD caps are typically sub-10 nm).[32,33] Experimental and continuum-scale analyses indicate that thicker dielectric films sustain confined pressure fields more effectively, promoting formation and retention of R8/BC8 phases under indentation; however, classical thin-film buckling and delamination theory shows that sufficiently large film stiffness/thickness and high compressive strains can instead promote buckling-driven delamination under severe contact loading. Thus, while a practical design window on the order of a few hundred nanometres (≈250–400 nm) often balances confinement with mechanical stability, the precise crossover depends on film microstructure, adhesion and indenter geometry and should be validated experimentally.[36,92]

The functional role of the oxide layer can be precisely characterized through elasticity theory as a stress-distribution boundary condition that modulates how applied loads are partitioned between elastic, plastic, and phase-transformation processes in the silicon substrate. This framework clarifies why the oxide does not alter critical transformation pressures (as confirmed by constant pop-out loads and critical pressures in Table 1) but profoundly affects transformation volumes and spatial distributions.

In bare Si the unloading stress decays rapidly, whereas bonding to a SiO_2 cap alters the surface boundary condition and slows stress relief. Our data and prior MD/experimental work indicate the oxide effectively acts as an additional elastic/viscoelastic constraint that lengthens the characteristic stress-decay time (τ) by a factor of order unity; the exact factor depends on oxide thickness, microstructure and loading geometry and should be measured directly for each system.[98] In bare Si, the unloading stress decays rapidly, causing the β-Sn phase to lose pressure before significant crystallization can occur, leading to predominantly amorphous products. In contrast, oxide-coated Si unloads more slowly due to the constrained boundary condition imposed by the film. This prolongs the interval during which high pressure is sustained, allowing β-Sn to transform into R8/BC8 before the stress fully dissipates.

Beyond the timescale argument, elasticity theory also predicts a spatial variation in the extent of high-pressure phases observed in TEM images (Fig. 4): the elastic constraint exerted by the oxide cap is strongest at the oxide–silicon interface and gradually weakens with depth into the silicon substrate, consistent with a decay of the constrained strain field over tens to a few hundreds of nanometres depending on oxide thickness and elastic mismatch. This depth-dependent constraint helps explain the layered phase distributions seen beneath the indenter.[18] In the oxide-coated spherical indent case (where the oxide remains intact), high confinement pressure extends to substantial depths, allowing R8/BC8 crystallization throughout the transformed zone (hence the uniform high-crystallinity distribution observed in TEM, Fig. 4c and d). In the Berkovich case (where oxide fractures early), confinement is breached at the surface, and confinement pressure decays rapidly with depth, creating the stratified structure observed: near-surface amorphization (no sustained confinement, rapid quenching) grading into deeper R8/BC8 (residual confinement, slower quenching). This spatial pattern, unique to the oxide-integrated system and absent in bare Si, represents direct experi-

mental evidence that oxide acts as a boundary condition governing stress distribution and relaxation kinetics, not as a pressure modifier altering the intrinsic transformation threshold.

The distinction between "boundary condition" and "pressure modifier" is critical for understanding the oxide's functional role. A pressure modifier would shift the β-Sn → R8/BC8 transformation threshold itself, raising or lowering the critical pressure at which the transition occurs. Our data decisively rule this out: pop-out loads (Table 1) match literature bare Si values (42 mN; literature 40–50 mN for Berkovich; 92 mN; literature 80–85 mN for spherical)[5,21,40] and calculated critical pressures align with published Si phase-diagram values. A boundary condition, by contrast, affects how the stress field is distributed spatially and temporally – how it evolves during loading and unloading – without changing the underlying thermodynamic thresholds. This is precisely what we observe: the oxide modulates the spatial location (surface-proximal *vs.* deep), volume (sustained development to 8–9 μm^3, similar to bare Si), and phase fractions (higher R8/BC8 percentage, lower amorphous percentage) of transformed regions without raising or lowering the transformation pressure. This conceptual clarity, distinguishing boundary effects from pressure effects, is the foundation for interpreting and engineering the oxide's functional role in stress-engineered silicon systems.

4.7 Implications for semiconductor systems

For oxide-coated semiconductor systems like our 285 nm SiO_2 on Si, the results carry important implications for device reliability and functionality. The silicon substrate retains its ability to undergo pressure-induced phase transformations even beneath a thin oxide film, meaning metastable high-pressure phases form under contact stresses typical in device operation, introducing residual stresses and potential instabilities. Pop-out events, while relieving elastic energy, introduce tensile stress from volume expansion during β-Sn → R8/BC8 transformation, which may accelerate cracking or delamination in adjacent regions. The oxide film acts as a sacrificial layer that cracks at lower loads than required for catastrophic substrate failure but provides minimal protection, true protection would require thicker, better-adhered, or inherently tougher films.[67,99]

Indenter geometry governs both reliability pathways and failure modes. Sharp contacts (Berkovich-like, resembling asperities or probes) induce early cracking and phase transformation at low loads, creating many distributed small cracks that cause gradual degradation. Blunt contacts (spherical, analogous to packaging stresses) allow quasi-ductile deformation *via* phase change, delaying catastrophic failure to higher thresholds, but risk sudden large-area delaminations when failure finally occurs.[26,100] Design strategies must address both scenarios, minimize sharp contacts and using buffer layers for distributed loads. Our results validate theoretical predictions by Lin *et al.*[101] that indenter geometry controls metastable phase formation in silicon, confirming this holds true for oxide-coated systems. The oxide modifies stress distribution and crack morphology but does not alter the fundamental transformation-fracture competition in silicon.

Beyond reliability, subsurface polymorphs possess direct optoelectronic value. R8 silicon exhibits reduced reflectance and enhanced refractive index, while BC8 shows narrower bandgaps and improved carrier mobility. Mannepalli *et al.*[102] demonstrated that wafer-integrated R8-Si enhanced solar absorption and photocurrent density by an order of magnitude, underscoring the optoelectronic potential of stress-stabilized buried phases for bandgap-engineered photonics, low-resistance MEMS contacts, and infrared detectors.[103,104]

Future studies should quantify interfacial adhesion *via* fracture mechanics methods and integrate finite element and molecular dynamics modeling to correlate stress fields, crack deflection, and phase boundary propagation. Raman stress mapping combined with theoretical modeling could clarify why sharp contacts localize transformation and fracture while spherical contacts distribute stress more diffusely, enabling rational design of semiconductor architectures for next-generation optoelectronic and sensing applications. Overall, our comprehensive data and literature synthesis confirm that the 285 nm oxide layer acts predominantly as a stress boundary condition, enhancing phase crystallization and transformation volumes without altering the fundamental transformation pressures.

5. Conclusion

This study reveals how contact geometry and oxide constraint cooperatively govern phase transformation and fracture in nanoindented silicon. By systematically comparing Berkovich and spherical indentation of 285 nm SiO_2-capped Si(100), combined with Raman spectroscopy, SEM, and cross-sectional TEM, we establish quantitative principles linking stress field geometry to subsurface deformation pathways. Berkovich indentation concentrates stress locally, triggering phase transformation at ~42 mN (consistent with bare Si literature values of 40–50 mN). However, this geometry also initiates early fracture; radial and lateral cracks appear at 40–50 mN, with severe oxide delamination by ~100 mN. The transformed zones contain a mix of crystalline R8/BC8 and amorphous regions, reflecting the competing effects of localized hydrostatic pressure and high deviatoric stress at the indent periphery.

Spherical indentation distributes stress more broadly, delaying transformation onset to ~92 mN (*cf.* bare Si: 80–85 mN). Once activated, this geometry generates substantially larger and more uniform transformed zones dominated by crystalline R8/BC8 with minimal amorphous content. Crucially, the distributed stress field suppresses fracture propagation; surface damage remains confined to ring cracks and shallow delamination even at loads ≥500 mN. The 285 nm oxide layer plays a dual role: it extends stress-relaxation kinetics during unloading, promoting crystalline phase formation over amorphization, while simultaneously acting as a weak interface susceptible to delamination.

Our comparison with high-load literature benchmarks reveals a fundamental limit to oxide confinement. While the SiO_2 cap stabilizes the β-Sn phase and promotes crystalline recovery at moderate spherical loads (~200 mN), the volumetric expansion associated with the transformation eventually overwhelms the capping layer at higher loads (~500 mN). This defines a specific "critical loading window" for successful subsurface phase engineering, where the benefits of hydrostatic pressure are maximized before strain accumulation drives the system toward amorphization and fracture.

These findings validate that oxide-constrained silicon behaves as a boundary-condition-controlled system rather than a pressure-modified one. The critical transformation pressure (~11–12 GPa) remains independent of oxide presence, confirming that the oxide modulates stress distribution and relaxation kinetics rather than thermodynamic thresholds. For device applications requiring large, stable subsurface R8/BC8 regions with minimal damage, spherical contacts within the identified critical loading window combined with oxide thicknesses of 200–350 nm are optimal. This work establishes the mechanistic foundation for designing stress-engineered silicon architectures with tailored subsurface optical and mechanical properties.

Author contributions

K. M. S. R. N. contributed to conceptualization and supervision. M. S. N. conducted the experiments and analysis and wrote the original and revised manuscript versions. Both authors have contributed to writing/correcting the final draft of the manuscript.

Conflicts of interest

The authors declare no conflict of interest.

Data availability

The data that support the findings of this study are available from the corresponding author upon reasonable request.

Supplementary information (SI) is available. See DOI: https://doi.org/10.1039/d5nr04069h.

Acknowledgements

Megha S. N. thanks the SRM Institute of Science and Technology for providing a fellowship to pursue doctoral studies. K. S. R. N. M. thanks the Science and Engineering Research Board, Government of India, for a Core Research Grant (no.: CRG/2020/1902). The authors acknowledge that SRM-IST central facilities and the Nanotechnology Research Centre (NRC) provide a few characterization facilities, as well as CeNSE, IISc, for providing the FIB facility. K. S. R. N. M. sincerely thanks Prof. Jim Williams and Prof. Jodie Bradby, Australian National University, for their valuable guidance.

References

1 M. A. Green, *Prog. Photovoltaics*, 2005, **13**, 447–455.
2 J. E. Bradby, J. S. Williams, J. Wong-Leung, M. V. Swain and P. Munroe, Materials Research Society Symposium-Proceedings, 2001, vol. 649, p. 810.
3 E. R. Weppelmann, J. S. Field and M. V. Swain, *J. Mater. Res.*, 1993, **8**, 830–840.
4 V. Domnich, Y. Gogotsi and S. Dub, *Appl. Phys. Lett.*, 2000, **76**, 2214–2216.
5 T. Juliano, V. Domnich and Y. Gogotsi, *J. Mater. Res.*, 2004, **19**, 3099–3108.
6 V. Domnich and Y. Gogotsi, *Rev. Adv. Mater. Sci.*, 2002, **3**, 1–36.
7 H. Olijnyk, S. K. Sikka and W. B. Holzapfel, *Phys. Lett. A*, 1984, **103**, 137–140.
8 J. Z. Hu, L. D. Merkle, C. S. Menoni and I. L. Spain, *Phys. Rev. B: Condens. Matter Mater. Phys.*, 1986, **34**, 4679.
9 J. Crain, G. J. Ackland, J. R. Maclean, R. O. Piltz, P. D. Hatton and G. S. Pawley, *Phys. Rev. B: Condens. Matter Mater. Phys.*, 1994, **50**, 13043.
10 J. C. Jamieson, *Science*, 1963, **139**, 762–764.
11 Y. Q. Wu, X. Y. Yang and Y. B. Xu, *Acta Mater.*, 1999, **47**, 2431–2436.
12 R. O. Piltz, J. R. MacLean, S. J. Clark, G. J. Ackland, P. D. Hatton and J. Crain, *Phys. Rev. B: Condens. Matter Mater. Phys.*, 1995, **52**, 4072.
13 L. Chang and L. C. Zhang, *Acta Mater.*, 2009, **57**, 2148–2153.
14 G. M. Pharr, W. C. Oliver and D. S. Harding, *J. Mater. Res.*, 1991, **6**, 1129–1130.
15 S. Jiapeng, L. Cheng, J. Han, A. Ma and L. Fang, *Sci. Rep.*, 2017, **7**, 10282.
16 I. Zarudi, J. Zou and L. C. Zhang, *Appl. Phys. Lett.*, 2003, **82**, 874–876.
17 J. Jang, M. J. Lance, S. Wen, T. Y. Tsui and G. M. Pharr, *Acta Mater.*, 2005, **53**, 1759–1770.
18 G. Ge, F. Rovaris, D. Lanzoni, L. Barbisan, X. Tang, L. Miglio, A. Marzegalli, E. Scalise and F. Montalenti, *Acta Mater.*, 2024, **263**, 119465.
19 H. Bei, E. P. George, J. L. Hay and G. M. Pharr, *Phys. Rev. Lett.*, 2005, **95**, 045501.
20 L. Ma, L. Levine, R. Dixson, D. Smith and D. Bahr, in *Nanoindentation in Materials Science*, 2012, pp. 25–82.
21 I. Zarudi, L. C. Zhang, W. C. D. Cheong and T. X. Yu, *Acta Mater.*, 2005, **53**, 4795–4800.
22 I. Zarudi, L. C. Zhang, J. Zou and T. Vodenitcharova, *J. Mater. Res.*, 2004, **19**, 332–337.
23 N. Souza Heinz, K. Wegener and Fabio Antonio Xavier, *Repositório Institucional da UFSC, Simulation of silicon machining with molecular dynamics*, 2023.

24 L. C. Zhang and H. Tanaka, *JSME Int. J., Ser. A*, 1999, **42**, 546–559.
25 A. S. Bhattacharyya, R. P. Kumar, S. Priyadarshi, Sonu, S. Shivam and S. Anshu, *J. Mater. Eng. Perform.*, 2018, **27**, 2719–2726.
26 R. F. Cook, *J. Mater. Sci.*, 2006, **41**, 841–872.
27 G. M. Pharr, W. C. Oliver and D. R. Clarke, *J. Electron. Mater.*, 1990, **19**, 881–887.
28 J. E. Bradby, J. S. Williams, J. Wong-Leung, M. V. Swain and P. Munroe, *Appl. Phys. Lett.*, 2000, **77**, 3749–3751.
29 M. I. McMahon and R. J. Nelmes, *Phys. Rev. B: Condens. Matter Mater. Phys.*, 1993, **47**, 8337.
30 W. Zhang, Y. Yang, D. Chen, T. Zhao, D. Li and Y. Yang, *Symmetry*, 2025, **17**, 46.
31 J. Chen, J. Shi, M. Zhang, W. Peng, L. Fang, K. Sun and J. Han, *Comput. Mater. Sci.*, 2018, **155**, 1–10.
32 J. Chen, L. Fang, M. Zhang, W. Peng, K. Sun and J. Han, *Acta Mech. Solida Sin.*, 2021, **34**, 506–515.
33 J. Chen, J. Shi, Y. Wang, J. Sun, J. Han, K. Sun and L. Fang, *RSC Adv.*, 2018, **8**, 12597–12607.
34 C. W. Kang and H. Huang, *Adv. Manuf.*, 2017, **5**, 1–19.
35 J. Ke, P. Ying, Y. Du, B. Zou, H. Sun and J. Zhang, *Phys. Chem. Chem. Phys.*, 2022, **24**, 15991–16002.
36 W. Zhang, J. Li, Y. Xing, X. Nie, F. Lang, S. Yang, X. Hou and C. Zhao, *Coatings*, 2021, **11**, 1–12.
37 F. Helvaci and J. Cho, *Mater. Res. Soc. Symp. Proc.*, 2005, **841**, R12.10.
38 M. S. R. N. Kiran, T. T. Tran, L. A. Smillie, B. Haberl, D. Subianto, J. S. Williams and J. E. Bradby, *J. Appl. Phys.*, 2015, **117**, 205901.
39 B. D. Beake, M. I. Davies, T. W. Liskiewicz, V. M. Vishnyakov and S. R. Goodes, *Wear*, 2013, **301**, 575–582.
40 T. Juliano, Y. Gogotsi and V. Domnich, *J. Mater. Res.*, 2003, **18**, 1192–1201.
41 S. Ruffell, B. Haberl, S. Koenig, J. E. Bradby and J. S. Williams, *J. Appl. Phys.*, 2009, **105**, 093513.
42 A. Kailer, K. G. Nickel and Y. G. Gogotsi, *J. Raman Spectrosc.*, 1999, **30**, 939–946.
43 S. Mannepalli and K. S. R. N. Mangalampalli, *J. Appl. Phys.*, 2019, **125**, 225105.
44 C. R. Das, H. C. Hsu, S. Dhara, A. K. Bhaduri, B. Raj, L. C. Chen, K. H. Chen, S. K. Albert, A. Ray and Y. Tzeng, *J. Raman Spectrosc.*, 2010, **41**, 334–339.
45 Y. B. Gerbig, C. A. Michaels, J. E. Bradby, B. Haberl and R. F. Cook, *Phys. Rev. B: Condens. Matter Mater. Phys.*, 2015, **92**, 214110.
46 W. E. Hong and J. S. Ro, *J. Appl. Phys.*, 2013, **114**, 073511.
47 R. Rao, J. E. Bradby, S. Ruffell and J. S. Williams, *Microelectron. J.*, 2007, **38**, 722–726.
48 M. S. R. N. Kiran, B. Haberl, J. E. Bradby and J. S. Williams, in *Semiconductors and Semimetals*, Academic Press Inc., 2015, vol. 91, pp. 165–203.
49 P. K. Kulshreshtha, K. M. Youssef and G. Rozgonyi, *Sol. Energy Mater. Sol. Cells*, 2012, **96**, 166–172.
50 S. Bhowmick, H. Cha, Y. G. Jung and B. R. Lawn, *Acta Mater.*, 2009, **57**, 582–589.
51 Z. Xia, W. A. Curtin and B. W. Sheldon, *Acta Mater.*, 2004, **52**, 3507–3517.
52 M. Sullivan and B. Prorok, Conference Proceedings of the Society for Experimental Mechanics Series, 2016, vol. 5, pp. 45–50.
53 I. Zarudi, L. C. Zhang and M. V. Swain, *Appl. Phys. Lett.*, 2003, **82**, 1027–1029.
54 H. Wan, Y. Shen, Q. Chen and Y. Chen, *J. Mater. Res.*, 2010, **25**, 2224–2237.
55 R. Dash, K. Bhattacharyya and A. S. Bhattacharyya, *Nanotechnol. Precis. Eng.*, 2023, **6**, 042001.
56 S. Wong, B. C. Johnson, B. Haberl, A. Mujica, J. C. McCallum, J. S. Williams and J. E. Bradby, *J. Appl. Phys.*, 2019, **126**, 105901.
57 B. Haberl, M. Guthrie, S. V. Sinogeikin, G. Shen, J. S. Williams and J. E. Bradby, *High Pressure Res.*, 2015, **35**, 99–116.
58 D. Ge, *TEM investigation of contact loading induced phase transformation in silicon*, Philadelphia, 2004.
59 S. Wong, B. Haberl, J. S. Williams and J. E. Bradby, *Appl. Phys. Lett.*, 2015, **106**, 252103.
60 A. B. Mann, D. Van Heerden, J. B. Pethica and T. P. Weihs, *J. Mater. Res.*, 2000, **15**, 1754–1758.
61 I. Zarudi, L. C. Zhang and M. V. Swain, *J. Mater. Res.*, 2003, **18**, 758–761.
62 M. Bikerouin, A. Marzegalli, D. Spirito, G. J. K. Schaffar, C. Bongiorno, F. Rovaris, M. Zaghloul, A. A. Corley-Wiciak, A. M. Mio, L. Miglio, V. Maier-Kiener, G. Capellini and E. Scalise, *Small Struct.*, 2025, **6**, 2400552.
63 M. Sasidharan Nisha, Y. Chandran, A. A. Sagade, V. Balakrishnan, A. Courac and K. Mangalampalli, *Adv. Funct. Mater.*, 2025, 2425188.
64 B. C. Johnson, B. Haberl, J. E. Bradby, J. C. McCallum and J. S. Williams, *Phys. Rev. B: Condens. Matter Mater. Phys.*, 2011, **83**, 235205.
65 S. Ruffell, J. E. Bradby and J. S. Williams, *Appl. Phys. Lett.*, 2007, **90**, 131901.
66 S. Yesudhas, V. I. Levitas, F. Lin, K. K. Pandey and J. S. Smith, *Nat. Commun.*, 2024, **15**, 7054.
67 Z. Zeng, Q. Zeng, W. L. Mao and S. Qu, *J. Appl. Phys.*, 2014, **115**, 103514.
68 A. A. Volinsky, N. R. Moody and W. W. Gerberich, *Acta Mater.*, 2002, **50**, 441–466.
69 D. Ge, V. Domnich and Y. Gogotsi, *J. Appl. Phys.*, 2003, **93**, 2418–2423.
70 J. E. Bradby, J. S. Williams, J. Wong-Leung, M. V. Swain and P. Munroe, *J. Mater. Res.*, 2001, **16**, 1500–1507.
71 N. Fujisawa, R. T. Keikotlhaile, J. E. Bradby and J. S. Williams, *J. Mater. Res.*, 2008, **23**, 2645–2649.
72 A. Kailer, Y. G. Gogotsi and K. G. Nickel, *J. Appl. Phys.*, 1997, **81**, 3057–3063.
73 S. Minomura and H. G. Drickamer, *J. Phys. Chem. Solids*, 1962, **23**, 451–456.
74 L. Zhang and I. Zarudi, *Int. J. Mech. Sci.*, 2001, **43**, 1985–1996.
75 S. Ruffell, J. E. Bradby and J. S. Williams, *Appl. Phys. Lett.*, 2006, **89**, 091919.

76 P. Ostojic and R. McPherson, *Int. J. Fract.*, 1987, **33**, 297–312.
77 B. R. Lawn and D. B. Marshall, *J. Res. Natl. Bur. Stand. (U. S.)*, 1984, **89**, 435.
78 D. J. Oliver, *Nanoindentation-induced Deformation Mechanisms in Germanium*, 2008.
79 K. P. Marimuthu, F. Rickhey, J. H. Lee and H. Lee, *J. Eur. Ceram. Soc.*, 2017, **37**, 381–391.
80 W. Zhou and F. Yang, *Int. J. Mech. Sci.*, 2022, **229**, 107512.
81 B. R. Lawn, *Proc. R. Soc. London, Ser. A*, 1967, **299**, 307–316.
82 X. Li, D. Diao and B. Bhushan, *Acta Mater.*, 1997, **45**, 4453–4461.
83 D. J. Oliver, B. R. Lawn, R. F. Cook, M. G. Reitsma, J. E. Bradby, J. S. Williams and P. Munroe, *J. Mater. Res.*, 2008, **23**, 297–301.
84 W. C. D. Cheong and L. C. Zhang, *Nanotechnology*, 2000, **11**, 173.
85 E. R. Weppelmann, X. Z. Hu, M. V. Swain and M. V. Swain, *J. Adhes. Sci. Technol.*, 1994, **8**, 611–624.
86 M. Lu, H. Xie and H. Huang, *Key Eng. Mater.*, 2013, **533**, 201–222.
87 S. R. Jian, *Nanoscale Res. Lett.*, 2008, **3**, 6.
88 B. Lawn and R. Wilshaw, *J. Mater. Sci.*, 1975, **10**, 1049–1081.
89 R. F. Cook and G. M. Pharr, *J. Am. Ceram. Soc.*, 1990, **73**, 787–817.
90 M. R. Marulli, J. Bonari, J. Reinoso and M. Paggi, *J. Mech. Phys. Solids*, 2023, **178**, 105345.
91 A. B. Mann, D. Van Heerden, J. B. Pethica, P. Bowes and T. P. Weihs, *Philos. Mag. A*, 2002, **82**, 1921–1929.
92 J. W. Hutchinson and Z. Suo, *Adv. Appl. Mech.*, 1991, **29**, 63.
93 C. Lin, X. Liu, D. Yang, X. Li, J. S. Smith, B. Wang, H. Dong, S. Li, W. Yang and J. S. Tse, *Phys. Rev. Lett.*, 2020, **125**, 155702.
94 J. E. Bradby, J. S. Williams and M. V. Swain, *Phys. Rev. B: Condens. Matter Mater. Phys.*, 2003, **67**, 085205.
95 W. Han, J. Yu and Q. Wang, *J. Appl. Phys.*, 2000, **88**, 4404–4406.
96 S. Ruffell, J. E. Bradby, N. Fujisawa and J. S. Williams, *J. Appl. Phys.*, 2007, 101.
97 S. Wong, B. Haberl, B. C. Johnson, A. Mujica, M. Guthrie, J. C. McCallum, J. S. Williams and J. E. Bradby, *Phys. Rev. Lett.*, 2019, **122**, 105701.
98 A. Boé, A. Safi, M. Coulombier, T. Pardoen and J. P. Raskin, *Thin Solid Films*, 2009, **518**, 260–264.
99 L. Yin, Y. Dai and H. Hu, *Silicon*, 2022, **14**, 5173–5178.
100 B. Huang, M. H. Zhao, C. F. Gao and T. Y. Zhang, *Scr. Mater.*, 2004, **50**, 607–611.
101 Y. H. Lin, S. R. Jian, Y. S. Lai and P. F. Yang, *Nanoscale Res. Lett.*, 2008, **3**, 71.
102 S. Mannepalli, A. A. Sagade and K. S. R. N. Mangalampalli, *Scr. Mater.*, 2020, **184**, 19–23.
103 J. H. Kim, H. J. Kil, S. Lee, J. Park and J. W. Park, *ACS Omega*, 2022, **7**, 25219–25228.
104 V. K. Khanna, *J. Phys. D: Appl. Phys.*, 2011, **44**, 034004.